OVERLAY

Journal of Theoretical, Computational and Applied Mechanics

JTCAM

DIAMOND OPEN ACCESS

Identifiers
DOI 10.46298/jtcam.9296
OAI hal-03628416v3

History
Received Apr 4, 2022
Accepted Sep 21, 2022
Published Feb 3, 2023

Associate Editor
Anna Pandolfi

Reviewer
Roberto Brighenti

Open Review
OAI hal-03963541

Supplementary Material
Figure Data
DOI 10.5281/zenodo.7576704

Fatigue crack growth under large scale yielding condition: a tool based on explicit crack growth

Vincent Maurel[1], Vincent Chiaruttini[2], Alain Köster[1], and Djamel Missoum-Benziane[1]

[1] MINES ParisTech, PSL University, MAT - Centre des Matériaux, CNRS UMR 7633, Evry, France
[2] Université Paris-Saclay, ONERA, Matériaux et Structures, Châtillon, France.

This paper is dedicated to our too early departed friend and colleague Alain Köster who was instrumental in outstanding experiments in the field of fatigue crack growth.

Fatigue crack growth under large-scale yielding condition is studied for high-temperature loading. The applied strains are so important that diffuse damage phenomena are visible as a network of micro-cracks in front of the major crack. The survey of a macroscopic cracked surface is nevertheless possible, and numerical simulations with explicit representation of this crack are carried out to evaluate crack driving forces. The proposed numerical scheme takes into account plastic wake in the course of crack growth in a 3D model. A non-local model of fatigue crack growth rate, based on partition of strain energy density into elastic and plastic terms, yields improved results as compared to classical assessment of ΔJ by numerical methods.

Keywords: low cycle fatigue, strain energy method, high temperature fatigue, non-local model, adaptive remeshing

1 Introduction

Fatigue crack growth under large scale yielding condition should be considered for many structures designed in the LCF regime. Cases could be separated in first macroscopic loading with LCF regime inducing sustained cyclic plasticity at the structure scale (e.g. combustion chambers, aerospace components, automotive turbocharger...), and second for crack initiated in region where large scale yielding is induced by stress concentration (e.g. pores, defects, local modification of the geometry...). Whereas in-depth analysis of short fatigue crack regime accounting for plasticity has been widely studied since the pioneering works (Miller 1982; Vormwald and Seeger 1991; Doring et al. 2006), most of long crack analyses under fatigue plastic regime correspond to limited plasticity (Vormwald 2013). Besides, for long crack associated to loading inducing large scale yielding, fatigue crack growth mechanisms differ to some extent from fatigue crack growth in small scale yielding condition. Main features observed for fatigue crack growth under large scale yielding can be summarized as follows:

- crack tip blunting is observed (Tanaka et al. 1984); see the red square in Figure 1;
- plastic wake increases with crack growth (Kolednik et al. 2014); see variation of contrast in Figure 1(a) and surface variations in Figure 2(b);
- for strain-controlled tests, negative stresses are observed yielding pronounced crack closure and plasticity in compression (Bhanu Sankara Rao et al. 1988);
- strain localization exceeds the crack vicinity up to so-called general scale yielding (Kolednik et al. 2014);
- microcracks are observed in the strain localization pattern before major crack increment (Maurel et al. 2017); see red square in Figure 1;
- both transgranular and intergranular cracking (e.g. for ferritic stainless steel tested at rather low temperature 300 °C (Maurel et al. 2009)), intergranular cracking (e.g. for Co-base superalloys

Nomenclature

Acronyms

CTOD	crack tip opening displacement
dof	degree-of-freedom
EDM	electro-discharge machining
FCGR	fatigue crack growth rate
FEA	finite element analysis
HCF	high cycle fatigue
LCF	low cycle fatigue
LEFM	linear elastic fracture mechanics
PLC	Portevin Le Chatelier
SENT	single edge notch tension
VER	representative element of volume

Symbols

ΔJ^*	ΔJ derived from G-θ method
$\Delta\varepsilon$	fatigue strain amplitude (total strain)
$\mathrm{d}a/\mathrm{d}N$	FCGR
ℓ_c	radius of the sphere for averaging strain energy
λ	normalizing parameter for FGCR based on partition of energy
R_ε	fatigue load ratio for strain-controlled test
$\underset{\sim}{\sigma}$	stress tensor
$\underset{\sim}{\varepsilon}_{\mathrm{e}}$	elastic strain tensor
$\underset{\sim}{\varepsilon}_{\mathrm{vp}}$	viscoplastic strain tensor
m	exponent for FCGR for Paris' law
m_{e}, m_{p}	exponent for FCGR: elastic and plastic parts
W_{e}, W_{p}	elastic and plastic strain energies
w_{e}, w_{p}	non-local elastic and plastic strain energies
w_{e}^*, w_{p}^*	non-local FCGR model parameters for elastic and plastic contributions

at very high temperature 900 °C (Maurel et al. 2017)), brittle particles failure (e.g. for cast Al-alloys (Dezecot et al. 2019))... are different sources of this micro-cracks pattern;

- the crack growth mechanism implies the coalescence of a major crack to a network of micro-cracks (Schweizer et al. 2011; Dezecot et al. 2017); see Figure 1(b).

Last but not least, when considering the major crack to micro-crack coalescence, it is worthy that the stress triaxiality play a key role in that process. Consequently, the mechanisms involved in fatigue crack growth reaching large and general scale yielding present similarities with ductile failure, consistently with observed high fatigue crack growth rate, see e.g. (Benzerga et al. 1999; Zhang et al. 2018).

To illustrate the above features, lets consider in situ observation of a high temperature test achieved for Ha188 Co-based superalloys, using a SENT specimen of 18 mm wide and a crack length a of about 3 mm (see testing and geometry details in Section 3), Figure 1. Large crack

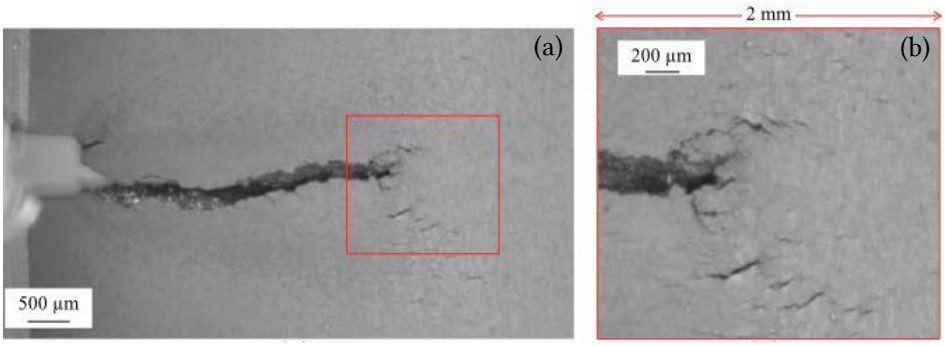

Figure 1 Observation of crack at maximum loading achieved in situ at 900 °C for Ha188 material using a SENT specimen (a) and detail of red square (b) for $\Delta\varepsilon/2 = 0.25\,\%$ and $R_\varepsilon = 0$.

opening is observed, Figure 1(a), together with evidence of crack tip blunting, Figure 1(b). Detailed view of the crack tip, thanks to in situ observation made at maximum applied load, evidences the micro-cracks network, in which the major crack is prone to grow, Figure 1(b). In this view, micro-cracks associated to the major crack in previous location are closed (previous location of the major crack corresponding to a lower number of cycles). This is due to the crack shielding effect of these micro-cracks by the major crack: only some traces of these micro-cracks can be observed in this static view. Reader has to refer to previous work to have detailed observation of this step by step process (Maurel et al. 2017; Trabelsi 2019).

For the same set of experiments, detailed in Section 3, plastic wake and transition from large to general scale yielding can be evidenced. For that purpose, roughness has been measured on one side of SENT specimens for increasing strain amplitude, see Figure 2. As a first approximation, these variations of surface roughness could be correlated to strain localization inducing local necking of the specimen. The increase of surface roughness, in both size and value, with increasing applied strain, illustrates the transition from relatively small scale yielding to general scale yielding condition. Besides, the fluctuation from positive to negative displacement observed

for the largest applied strain, $\Delta\varepsilon/2 = 0.45\,\%$ Figure 2(c), is associated to flat to slant evolution of the crack. This crack twisting (corresponding to a crack rotation around the direction of crack propagation) is again a characteristic of general scale yielding. The observed necking implies that 3D model should be achieved to take into consideration this effect on crack behaviour. The question of a criterion able to describe fatigue crack growth rate associated to these mechanisms is still open.

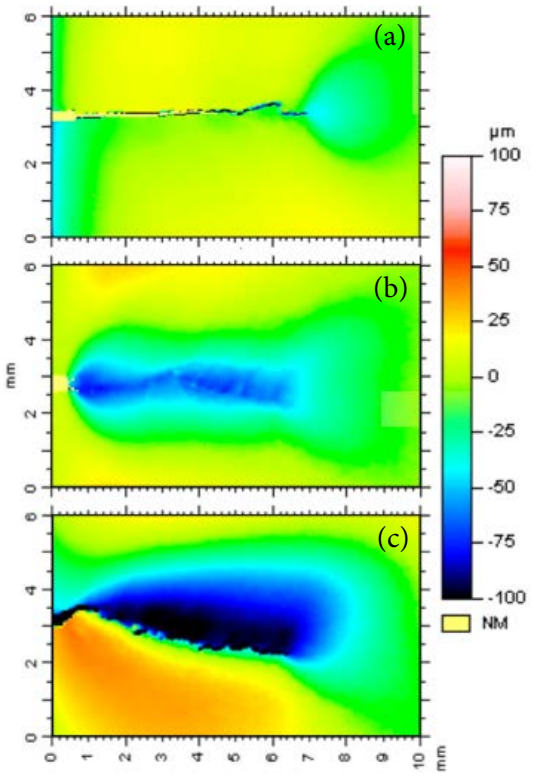

Figure 2 Measurements of surface roughness for (a) $\Delta\varepsilon/2 = 0.0625\,\%$, (b) $\Delta\varepsilon/2 = 0.25\,\%$ and (c) $\Delta\varepsilon/2 = 0.45\,\%$ and $R_\varepsilon = 0$. Adapted from (Trabelsi 2019). SENT specimen corresponding to Figure 3.

Furthermore, new tools are now available to describe in a robust manner fatigue crack growth based on either X-FEM technique (Ribeaucourt et al. 2007) or conform remeshing technique (Chiaruttini et al. 2012; Vattré and Chiaruttini 2022) to describe explicit 3D crack shape and its evolution with fatigue crack growth. For elastic-plastic material, the preservation of the internal variables being essential, both the sub-cutting technique of the X-FEM methods and conformal remeshing are requiring sounded field transfer operations. Furthermore, this FEA crack simulation process has already been successfully applied to a wide range of cases, in the scope of LEFM based on G-θ analysis (Destuynder et al. 1981; Suo and Combescure 1992; Fessler et al. 2017; Maurel et al. 2020).

This paper develops a 3D FEA method to describe evolution of crack from small to general scale yielding condition in fatigue and proposes fatigue crack growth rate criterion relevant to this context. The paper is organized as follows: a review of some criteria highlights their strength and weakness, then experimental details are recalled from a previous paper, this set of experiments being used for model identification. The core of the paper being the methodology of crack growth modelling, based on conform remeshing technique accounting for plastic wake, and the definition of a FCGR model based on partition of strain energy into elastic and plastic contribution. The paper concludes with some guidelines for FCGR in the context of FEA and simplification made for FCGR model.

2 Short review of FCGR criteria applied to general scale yielding

From the fatigue crack mechanisms detailed above, the question of driving forces for fatigue crack growth under large to general scale yielding could be analyzed through simplified energetic approach. Basically, the total potential energy of an isolated system Π can defined as the sum of its elastic energy Π_e, its plastic dissipation Π_p, and any other sources of dissipation Δ (Doudard

et al. 2005):

$$\Pi = \Pi_e + \Pi_p + \Delta. \tag{1}$$

Besides, within the scope of dissipation analysis, it has been widely commented that the dissipation is shared into self-heating and damage process (Charkaluk et al. 2002). On the other hand, within the scope of LEFM concepts, the elastic strain energy is assumed to be stored into the material, being releasable for crack growth.

These energetic analyses combined to observations of fatigue crack growth mechanisms from small to general scale yielding conditions are helpful to establish some conclusions: i) in small scale yielding condition, elastic model are convenient, by the way most of stored elastic energy remains available for fatigue crack growth ii) in general scale yielding conditions, the presence of micro-cracks pattern should be a source of dissipation by damage iii) transition from small to general scale yielding conditions questions the energy fluxes and iv) plasticity induces complex residual stress state function of crack growth and subsequent stress redistribution.

Both the experimental features of large to general scale yielding fatigue crack growth, and the above analysis of driving forces for crack growth could be useful to achieve a short overview of models for FCGR assessment in this context.

A general form, of a fatigue crack growth model is $\mathrm{d}a/\mathrm{d}N = f$ (driving force). The driving forces proposed by authors depend on several aspects, including fatigue domain, HCF or LCF, the possibility of assessment in linear elasticity, non linear elasticity, and general visco-plastic materials, describing short or/and long crack behavior. Some contributions of FCGR models suitable for LCF are listed in Table 1.

Model expression f	driving force	crack	non-local	reference
$C\Delta J^m$	ΔJ	short/long	yes	Dowling and Begley (1976)
$C(\Delta\mathrm{CTOD})^m$	$\Delta\mathrm{CTOD}$	long	yes	McMillan and Pelloux (1970)
$\alpha B\Delta\varepsilon_p a$ with $B = 1/\cos(\pi\Delta\sigma/(4T)) - 1$	$\Delta\sigma$ and $\Delta\varepsilon_p$	long	no	Tomkins (1968)
$C\Delta K_\varepsilon^m$ with $\Delta K_\varepsilon = f(a)\Delta\varepsilon\sqrt{\pi a}$	$\Delta\varepsilon_t$	short/long	no	Haigh and Skelton (1978)
$W_p(\mathrm{cum}) \geqslant W_{cr}(^*)$	$W_p(\mathrm{cum})$	long	yes	Cojocaru and Karlsson (2009)
$\lambda\left[\left(\frac{w_e}{\gamma_e}a\right)^{m_e} + \left(\frac{w_p}{\gamma_p}a\right)^{m_p}\right]$	W_p and W_e	long	no	Maurel et al. (2009)
	W_p and W_e	short/long	yes	Maurel et al. (2017)

Table 1 Model review, $\mathrm{d}a/\mathrm{d}N = f$ (driving force); (*) the criterion is related to the failure of one finite element (details in the core of the text).

In addition to these aspects, two main points should be considered in the scope of 3D FEA. First, FCGR models are either local or non-local, however this point is a requirement to limit the mesh dependency of FCGR assessment. Exception made of J and CTOD based models, most models consider a stress or a strain amplitude, associated to non-linear elasticity to mimic viscoplastic behavior (Haigh and Skelton 1978; Kamaya 2015; Cussac 2020; Cussac et al. 2020; Ravi Chandran 2018). This constitutes a second drastic limitation, considering FEA for structure applications.

On the other hand, strain energy models are straightforward for any mechanical behavior in the framework of standard generalized materials (Chaboche 1993). It could be either based solely on plastic strain energy (Cojocaru and Karlsson 2009) or on a partition of strain energy into elastic and plastic contributions (Maurel et al. 2009; Maurel et al. 2017). These latters are consistent with general observation in fatigue life similarly to Manson-Coffin partition of mechanical strain into elastic and plastic terms (Manson 1953; Coffin 1954), and will be detailed in the sequel.

The most standard model is based on energy release rate, assumed to be equivalent to integral J amplitude, ΔJ (Dowling and Begley 1976). The associated model was:

$$\frac{\mathrm{d}a}{\mathrm{d}N} = C\Delta J^m \quad \text{where} \quad \Delta J^m = \int_\Gamma \left(\Delta W\,\mathrm{d}y - \Delta\underset{\sim}{\sigma}\cdot\underline{n}\frac{\partial\Delta u}{\partial x}\,\mathrm{d}s\right) \text{ and } \Delta W = \int_0^{\Delta\varepsilon} \Delta\underset{\sim}{\sigma} : \mathrm{d}(\Delta\underset{\sim}{\varepsilon}) \tag{2}$$

with C and m, the models parameters, Γ, the contour chosen for integration, W, the total strain energy and $\underline{n}$, the vector normal to the contour Γ, as detailed in (Vormwald 2013). This model has been successfully identified for relatively low strain amplitude for isothermal fatigue crack growth, see e.g. (Haddar et al. 2013). The driving force for fatigue crack growth being either ΔJ as proposed by Dowling and Begley (1976) or a decomposition into elastic and plastic contribution, namely $\Delta J = \Delta J_e + \Delta J_p$ (Shih and Hutchinson 1976). These models are based on the underlying framework of non-linear elasticity, which is not able to model a wide range of materials. It is worth noting that on these basis, associating macroscopic analysis of a given specimen and non linear elasticity assumption, specific analytical formulations are able to describe short fatigue crack growth (Vormwald 2013). However, the question of adaptation of these models to structure are not fully addressed. To get rid of this limitation, numerical model to assess ΔJ are needed, among which the G-θ method is straightforward. This point will be detailed in Section 4.4. However, for long crack and general scale yielding condition, Kolednik et al. (2014) have clearly evidenced that strain localization initiated on crack tip could interact with other strain localization sources in the considered structure, resulting in the lost of consistency of invariance assumption for contour integral (Kolednik et al. 2014; Simha et al. 2008; Ochensberger and Kolednik 2015): modifying the integration contour, the numerical evaluation of ΔJ will be modified.

On the other hand, in the LCF regime, the interest in plastic strain energy, namely Δw_p as an indirect measurement of dissipation has been widely documented for life model based on initiation criterion (Charkaluk et al. 2002). Cojocaru and Karlsson (2009) and Nittur et al. (2014) have proposed a numerical scheme based on FEA, modeling a priori the crack shape with crack increase driven by debonding of nodes in the crack path, when the crack extension criterion is reached (Cojocaru and Karlsson 2009; Nittur et al. 2014). This criterion is based on the plastic strain energy, W_p, considered as the driving force for fatigue crack growth, see Figure 4(b), which is able to account for overload model in the Paris regime (Smith 2011; Nittur et al. 2013). The associated model was the following: a crack increment Δa is considered if $W_p(\text{cum}) \geqslant W_{cr}$, with $W_p(\text{cum}) = \sum w_p^{elt}$, w_p^{elt} being the plastic strain energy in elements located in a chosen domain used for non-local averaging, and W_{cr}, the critical energy at crack propagation being the model parameter. Indeed, the plastic strain energy is accumulated cycle by cycle up to reaching the failure criterion for a given crack increment. The numerical scheme is robust but is limited to a priori known crack path, and the FCGR model questions the way to reach general scale yielding condition with a single parameter approach.

To obtain a clear distinction of driving forces for fatigue crack growth between small scale yielding and general scale yielding, the partition of strain energy into elastic opening strain energy and distortion plastic strain energy has been proposed (Maurel et al. 2009). The basic idea is that both stored elastic strain energy and dissipated plastic strain energy contribute to crack growth. However, the amount of plastic strain energy available for crack growth could not be of the same order of magnitude as compared to elastic strain energy, because of dissipation into self heating, plastic straining and micro-cracks network processing. The associated model was:

$$\frac{\mathrm{d}a}{\mathrm{d}N} = \lambda\left[\left(\frac{W_e}{\gamma_e}a\right)^{m_e} + \left(\frac{W_p}{\gamma_p}a\right)^{m_p}\right] \tag{3}$$

where

$$W_e = \frac{1}{3}\int_{\text{cycle}} \langle \text{tr}\,\underset{\sim}{\sigma}\rangle \cdot \langle \text{tr}(\mathrm{d}\underset{\sim}{\varepsilon}_e)\rangle \quad \text{and} \quad W_p = \int_{\text{cycle}} \underset{\sim}{s} : \mathrm{d}\underset{\sim}{\varepsilon}_{vp} \tag{4}$$

with a, the crack length, W_e and W_p, the elastic and plastic strain energy, respectively, γ_e and m_e along with γ_p and m_p the models parameters associated to elastic and plastic contributions, respectively. The parameter λ is used only to address consistency in units. For strain energy definition, the authors proposed to use $\underset{\sim}{\sigma}$, $\underset{\sim}{\varepsilon}_e$ and $\underset{\sim}{\varepsilon}_{vp}$ corresponding respectively to stress, elastic strain and viscoplastic strain tensors. The trace of tensor is symbolized by tr, and $\langle\cdot\rangle$ corresponds to the Macaulay brackets, e.g. $\langle \text{tr}\,\underset{\sim}{\sigma}\rangle = \text{tr}\,\underset{\sim}{\sigma}$ if $\text{tr}\,\underset{\sim}{\sigma} > 0$ and $\langle \text{tr}\,\underset{\sim}{\sigma}\rangle = 0$ otherwise. Considering uniaxial condition, W_e corresponds to the area below positive elastic loading curve,

depicted as the grey area in Figure 4(b) while W_p corresponds to the total area delineated by the hysteretic curve, depicted as the dashed area in Figure 4(b). The enrichment of the above model considering partitioned strain energy into elastic and plastic terms, together with their distinction in contribution to FGCR, yields only two additional material parameters to be identified (γ_e, m_e, γ_p and m_p) as compared to general formulation (C and m, e.g. Equation (2)), the choice of the λ parameter, being not independent to the set of other parameters, does not modify the quality of the model identification. This model has been successfully applied for strain controlled tests for ferritic stainless steel (Maurel et al. 2009), Ni based superalloys (Heudt 2013) and Al cast alloys (Dezecot et al. 2019), for uniaxial and multiaxial loading with either sustained plasticity or decreasing loading conditions (Trabelsi 2019; Heudt 2013; Dezecot et al. 2019).

This first model was considering only macroscopic stress and strain state at the specimen length, i.e. strain energies were derived from either experimental values or RVE analysis. The strain energies were deduced for the former from stress-strain hysteretic curve, and for the latter from simulation using constitutive equations of the tested material. This prescribes the use of shape factor to account for specimen geometry (Maurel et al. 2009). This point questions the ability of the model to address structure application. Thus a simple non-local model using volume averaging, was proposed to model FCGR from small to general scale yielding condition (Maurel et al. 2017). The associated model was

$$\frac{\mathrm{d}a}{\mathrm{d}N} = \lambda\left[\left(\frac{w_e a}{\gamma_e(\ell_c)}\right)^{m_e} + \left(\frac{w_p a}{\gamma_p(\ell_c)}\right)^{m_p}\right] \quad \text{with} \quad w_e = \frac{1}{\Omega}\sum_{i=1}^{n} W_e\,\mathrm{d}\Omega_i \text{ and } w_p = \frac{1}{\Omega}\sum_{i=1}^{n} W_p\,\mathrm{d}\Omega_i \tag{5}$$

where W_e and W_p, defined in Equation (4), are determined locally for each of the n integration points within the volume Ω. Also, w_e and w_p correspond to the non-local strain energy, using a volume averaging of elastic and plastic strain energies based on finite element shape function. Others parameters being the same as developed in the first "macroscopic" version of the model detailed in Equation (3). The non-local approach implies to characterize the evolution of material parameters $\gamma_e(\ell_c)$ and $\gamma_p(\ell_c)$ as a function of the non-local length ℓ_c corresponding to the size of the box used for direct averaging of strain energy. By this way, the model becomes independent to the mesh size, typically for element sized below the non-local length ℓ_c. Besides, this model enables to describe local phenomenon, associated to short crack using refined mesh—e.g. crack to pore interaction (Dezecot et al. 2017)—as well as quick evaluation of FCGR, using coarse meshing (Heudt 2013). However, this non-local model was limited to notch plasticity analysis, without explicit model of crack growth and subsequently no analysis of plastic wake and stress redistribution with the crack growth.

To conclude with this review, FCGR models could be divided into different classes:

- Paris like or ΔJ models: limited by underlying assumption of non linear elasticity;
- strain or dissipated energy based model: a priori limited to cover the whole range from small to general scale yielding condition based on a single driving force term;
- partition of strain energy based models, tested only in notch plasticity cases without explicit crack growth,
- non-local models relevant within the scope of FEA (including ΔJ assessed by G-θ).

These last two points are the aim of this paper and will be addressed herein.

3 Experimental conditions

The chosen material, specimens and experimental conditions have been fully detailed in (Maurel et al. 2017). Thus, only major aspects will be briefly given here. The material used in this study is the high temperature Co-based superalloys Ha188 widely studied in the scope of high temperature LCF life, see e.g. (Bhanu Sankara Rao et al. 1997), which composition is detailed in Table 2.

SENT specimens have been machined from round bars, notch being processed by EDM, the width of the specimen being 18 mm, for a thickness of 4 mm and a notch sized to 900 µm, see Figure 3. The temperature was set to 900 °C controlled by a K-type thermocouple welded to the specimen, heating being obtained by a lamp furnace. All tests have been strain controlled using

Element	Co	Cr	Ni	W	C	La	Si	Fe	Mn
Weight (%)	Base	22.75	21.85	14.80	0.071	0.08	0.33	2.31	0.94

Table 2 Chemical composition of Ha188 superalloy used in the present study (wt %).

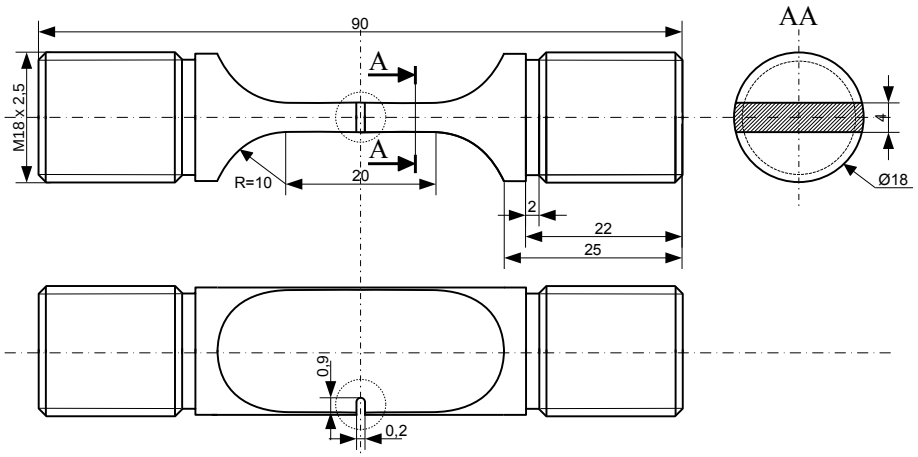

Figure 3 Representative sketch of the SENT specimen with enlarged notched area.

a contact extensometer located on the opposite side of the notch. The tested conditions are presented in Table 3.

Table 3 SENT test series conditions, number of cycles $N_{\max}$ to reach a crack length of 5 mm for SENT specimen (Maurel et al. 2017).

$\Delta\varepsilon/2$ (%)	Test frequency (Hz)	R_ε	$N_{\max}$
0.0625			4106
0.125			510
0.25	0.1	0	244
0.375			168
0.45			124

The crack length was measured by potential drop technique, calibrated with in situ optical microscope using Keyence VHX1000 system. To isolate the lens from heating and to limit air fluxes through the window used for observation, a quartz glass was glued to the external wall of the lamp furnace (Maurel et al. 2017).

In Figure 2, the surface roughness measurements show large variation of the surface local height with the crack growth which are strongly correlated to the local level of accumulated plasticity and crack plastic wake. Out-of-plane roughness corresponds to flat to slant transition of the crack, that is to say crack twisting increasing with the crack length, inducing multiaxial loading and mode mixity (Maurel et al. 2017; Maurel et al. 2020). The crack observation, and detailed analysis of the crack tip highlights a microcracks' network which is consistent with the path of strain localization, see Figure 1. The micro-crack pattern observed in Figure 1 corresponds to the same specimen where roughness has been measured in Figure 2(b). It is worth noting that the size of the area of significant variation of surface roughness (here of about 25 to 50 µm of depression) is consistent with the size of micro-cracks pattern. This point stresses out that large plasticity induces damage like localization.

Because of this microcracks' network, the measured crack length by potential drop technique includes these cracks. Thus, it is rather difficult to determine how the microcracks' network impact this measurement. This is the reason why we will only consider in the sequel the crack length of the major crack including the initial notch length, see arrow a in Figure 1(a), measured by optical microscope. The images have been triggered to maximum applied loading in the course of the cycling so as to measure the crack length when the crack is fully open.

The range of applied strain is correlated to macroscopic elastic behavior for $\Delta\varepsilon/2 = 0.0625\,\%$, to significant hysteresis for $\Delta\varepsilon/2 \geqslant 0.25\,\%$ and large hysteresis at maximum strain, $\Delta\varepsilon/2 = 0.45\,\%$, for which stress jumps are observed, Figure 4(a). The latter are associated to dynamic strain aging, the so-called PLC effect, already observed for this material (Lee et al. 1998).

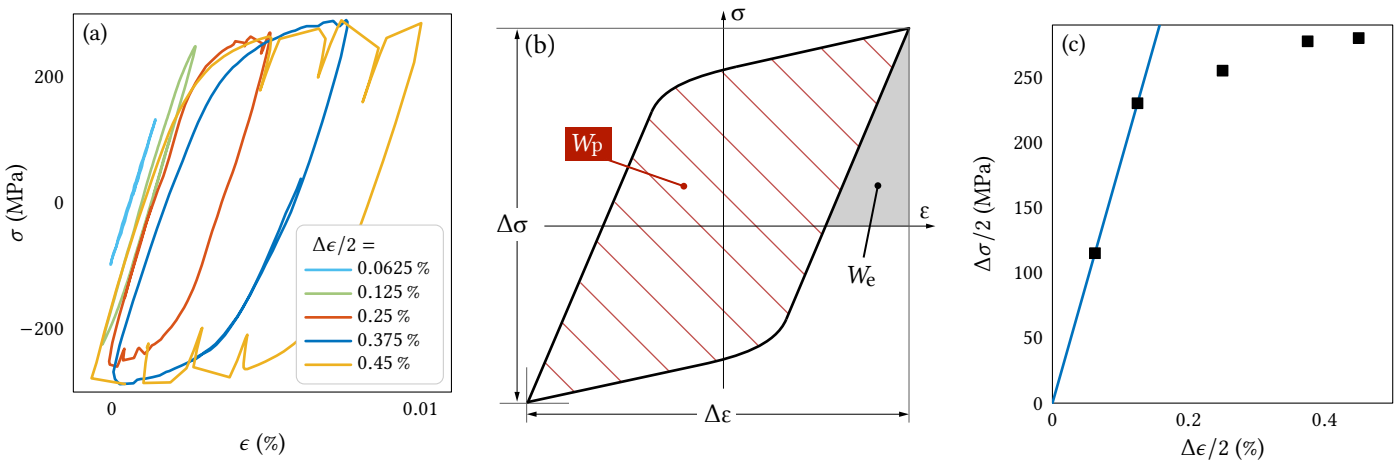

Figure 4 SENT specimens tested at 900 °C for a crack length of about 2 mm: (a) experimental stress-strain evolution, (b) schematic evolution and associated energies, stress and strain amplitudes and (c) experimental evolution of half amplitude stress and strain: black dots correspond to experimental values and blue line highlights the linear relationship between stress and strain for small scale yielding condition. See Table 3 for details.

However, large scale yielding is consistent with "sustained" plasticity exhibited by stress-strain macroscopic hysteresis curves. Besides, from this measurement, corresponding to a given crack length (here of about 2 mm), it is possible to plot the half variation of stress amplitude, $\Delta\sigma/2$, as a function of applied half strain amplitude, $\Delta\varepsilon/2$, Figure 4(c). The associated curve delineates a transition between small scale yielding condition, with a linear relationship between cyclic stress to cyclic strain, and general scale yielding condition for which the linearity is lost. The associated "life" considering the number of cycles to reach 5 mm, equivalent to 40 % of the width of the specimen, corresponds to LCF regime in the range 100–4000 cycles, see Table 3.

4 Numerical model

FEA was conducted using the finite element code Zset (Mines ParisTech and ONERA 2021).

4.1 Model behavior for Ha188

To describe the mechanical behavior of Ha188 superalloy, it has been shown that using constant isotropic and non linear kinematic hardening associated to Norton flow was straightforward at high temperature, ignoring the PLC effect for sake of simplicity (Chaboche et al. 2013). Two different potentials, respectively associated to a "quick" and a "slow" terms, are sufficient to model frequency effect, as validated in previous studies (Chaboche et al. 2013; Maurel et al. 2017). Thus equations are briefly recalled in Table 4.

Strain partitioning	$\underset{\sim}{\varepsilon}^{\text{tot}} = \underset{\sim}{\varepsilon}^{e} + \underset{\sim}{\varepsilon}^{p}$
Yield function	$f = \sqrt{\frac{3}{2}(\underset{\sim}{s} - \underset{\sim}{X}) : (\underset{\sim}{s} - \underset{\sim}{X})} - R - \sigma_y$
Kinematic Hardening	$\dot{\underset{\sim}{\alpha}} = \dot{\underset{\sim}{\varepsilon}}^{p} - \gamma \underset{\sim}{\alpha} \dot{p}$, $\dot{\underset{\sim}{X}} = \frac{2}{3} C \dot{\underset{\sim}{\alpha}}$
Isotropic Hardening	R = constant
Flow Function	"quick" term $\dot{p}_{\text{q}} = \langle f/K_N^q \rangle^{N^q}$, "slow" term $\dot{p}_{\text{s}} = \langle f/K_N^s \rangle^{N^s}$
Total accumulated plasticity	$\dot{p} = \dot{p}_{\text{q}} + \dot{p}_{\text{s}}$

Table 4 Mechanical behavior set of equation used for Ha188.

4.2 Geometry, boundary conditions and element assumptions

The chosen mesh is deduced from measured specimen geometry, accounting for realistic 3D shape of the specimen, including the notch and simplifying the zone used for gripping system

considering only cylindrical shape, Figure 5.

In the initial condition, an elliptical crack has been inserted in the mesh by conform remeshing technique using the Meshgems Software solution (Distene 2021). The ellipse dimensions and location are chosen so as to obtain a quasi linear crack with an initial crack length of 100 µm in addition to the notch. For sake of clarity, the mesh detailed in Figure 5(b) corresponds to a crack extension of 500 µm, geometrical parameters corresponding to Figure 3.

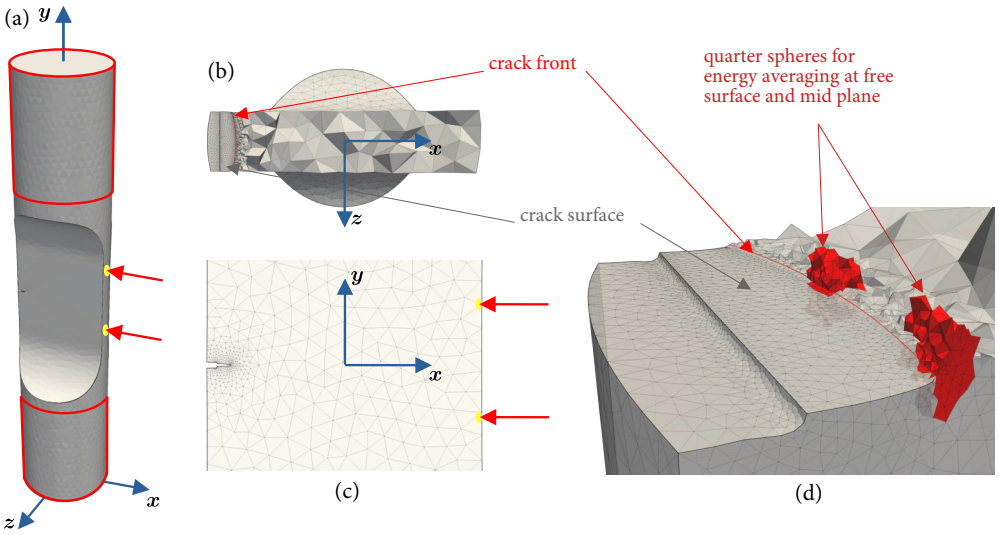

Figure 5 Sketch of geometry, crack and boundary conditions used for FEA: (a) perspective view where sets of nodes used for prescribed displacement are contoured in red, (b) cropped top-view revealing the crack inserted crack, (c) side-view exhibiting both notch and crack and (d) quarter sphere set of elements used for strain energy averaging in red; in all views thick red arrows ended by yellow points correspond to nodes used for controlled displacement to mimic extensometer.

All the simulations (after initial crack insertion and during the crack growth study) are performed using quadratic tetrahedron elements. The loading to be modelled by FEA corresponds to very high strain level, and subsequent high strain rate, in the specimen and especially in the crack front vicinity. To avoid oscillation of stress field, the quadratic elements are enriched by an additional dof controlling the pressure and the volume change, namely P_n, to subsequently insure the convergence of the trace of the stress tensor and triaxiality (e.g. see Zhang et al. (2018)). The minimal mesh size is set to $h = 50$ µm near the crack front and gradually increased up to 1 mm, yielding about 350×10^3 dofs including the pressure field P_n.

In order to mimic the grip system, the boundary conditions are based on prescribed homogeneous displacement on nodes corresponding to screwed part of the specimen on top surface in the y-direction, and zero displacement on the bottom surface, see red contours in Figure 5(a). The magnitude of the applied displacement is prescribed to respect the displacements of the nodes corresponding to the points of contact with the extensometer in order to represent the real strain prescribed experimentally, see red arrows ending with yellow points in Figure 5(a) and (c). A closed loop monitors the displacement of the top part of the specimen, so as to respect the targeted displacement between this pair of nodes, the displacement being derived from experimental strain accounting for the initial distance between these nodes. The implicit convergence is controlled by a Newton-Raphson algorithm.

The contact between the crack lips is managed through a node to face penalisation based contact algorithm, that neglects any friction between each side of the crack surface.

4.3 Crack growth, remeshing and internal variables

Mostly described for linear elastic cases in (Vattré and Chiaruttini 2022), the proposed method is an extension to non-linear explicit fatigue crack growth of the algorithms developed in the Z-set code, based successively for each crack increment on:

(i) FATIGUE FEA: fatigue loading cycling that takes into account crack closure effect and contact;
(ii) POST-PROCESSING: applying some post-processing computation on the FEA solution of the

balanced domain, to obtain useful dissipation parameters involved in the studied crack growth model;

(iii) PROPAGATION LAW: generating a crack front extension built on increment corresponding to the crack front speed at control points chosen along the crack front;

(iv) REMESHING: the remeshing of a given set of elements with conform remeshing of the new generated crack front location accordingly to control point increments;

(v) FIELD TRANSFER: the projection of the fields of displacement and internal variables from the previous mesh to the new mesh (which includes the crack growth), evaluated at the end of the current computed cycle, allowing to continue the calculation at the next iteration starting from such initial state.

This algorithm is illustrated in Figure 6(a).

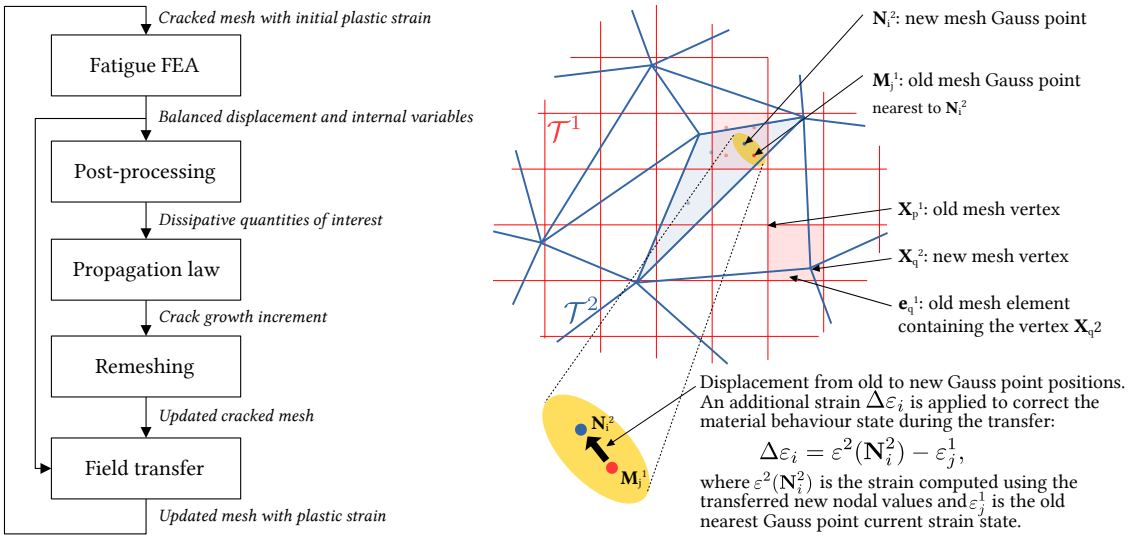

(a) Crack propagation algorithm **(b)** Data transfer correction process for integration points

Figure 6 Algorithm and mesh transfer details for large scale yielding crack growth.

For the initial crack, a few loading cycles can be applied to generate a more realistic and stabilised plastic strain field. However, the intent is to analyze crack propagation, which is also an effective way to account for stress re-equilibrium after each crack increment. Moreover, the chosen crack propagation procedure preserves internal variables state. As a consequence, a realistic stabilised plastic fatigue crack closure effect will be obtained after some propagation increments. Thus, only one cycle has been computed at each crack increment.

The evaluation of the crack increment is based on a G-θ analysis and Paris-like law described in the sequel, which corresponds to the common practice for small scale yielding condition and has been already integrated in the Zset code as a standard routine. By this way, the maximum crack increment $\Delta a_{\max}$ will correspond to the location where a maximum value of ΔJ, $\Delta J_{\max}$, is reached. An explicit linear approximation of the associated number of cycles $\Delta N = \Delta a_{\max}/(\mathrm{d}a/\mathrm{d}N)_{\max}$ is used with $(\mathrm{d}a/\mathrm{d}N)_{\max} = C(\Delta J_{\max})^m$. The crack increment for this prescribed ΔN number of cycles is thus computed for any other control points along the crack front.

During the transfer process, the projection of the internal variables state is based on the nearest Gauss point from old mesh to the new mesh, while the collocation of the new mesh nodes to old ones is used to get the values of the displacement field, using the old mesh base functions to get nodal values at the new mesh vertices coordinates. To insure the consistency between any Gauss point and the transferred nodal strain field, a correction is performed: it consists in prescribing the additional strain $\Delta\varepsilon$ mismatch to every integration point, as illustrated in Figure 6(b) (for a transfer between an old mesh $\mathcal{T}^1$ to a new one $\mathcal{T}^2$).

The mesh size is set to $h = 50\,\mu$m and the maximum crack increment $\Delta a_{\max}$, to $25\,\mu$m. This yields a satisfactory compromise between mesh quality and quality of fields of internal variables within the element after field projection. To improve the result quality, the chosen crack increment is much lower than the process zone associated to cyclic plastic radius. To compute a crack growth of 5 mm at the mid-plane of the specimen, 200 propagation steps have to be calculated.

4.4 ΔJ from G-θ

To evaluate the driving force associated to domain integral, J is evaluated through the so-called G-θ method. This method is based on a domain integral as originally proposed by Destuynder et al. (1981) and further developed by Suo and Combescure (1992). To limit domain dependency in the presence of plasticity and FEA simulation, a domain integral is achieved in the volume Ω. For large and general-scale yielding conditions, the classical J integral is known to become path dependent. Thus, as proposed by Simha et al. (2008), an extended J^* integral is defined as follows for incremental plasticity:

$$J^* = \int_\Omega \frac{1}{2}(\underset{\sim}{\sigma} : \underset{\sim}{\varepsilon}_e)\,\mathrm{tr}(\nabla\theta) - \mathrm{tr}(\underset{\sim}{\sigma}\nabla u\nabla\theta) - \underset{\sim}{\sigma} : \nabla\underset{\sim}{\varepsilon}_{ae}\cdot\theta\,\mathrm{d}\Omega \tag{6}$$

where tr is the first invariant of the considered tensor, $\underset{\sim}{\varepsilon}_e$ corresponds to the elastic strain tensor, $\underset{\sim}{\varepsilon}_{ae}$, to the anelastic strain tensor, $\nabla\underset{\sim}{\varepsilon}_{ae}$, to its gradient, $\underset{\sim}{\sigma}$, to the stress tensor. Also, ∇u is the gradient of the displacement field u and $\nabla\theta$ is the gradient of virtual increment of displacement of the crack front θ. Here, $\underset{\sim}{\varepsilon}_{ae} = \underset{\sim}{\varepsilon}_{tot} - \underset{\sim}{\varepsilon}_e - \underset{\sim}{\varepsilon}_{th}$, where $\underset{\sim}{\varepsilon}_{th}$ corresponds to the thermal strain tensor.

Including the term $\underset{\sim}{\sigma} : \nabla\underset{\sim}{\varepsilon}_{ae}\cdot\theta$, this formulation yields independence of J^* assessment to the domain chosen for integral when at least the first two elements are included in the domain using a FEA solution. The chosen domain was thus set to contain at least three layers of elements attached to the crack front. For cyclic loading, those J^* values are simply computed at both lower and upper values of the applied fatigue loading conditions, the resulting amplitude is

$$\Delta J^* = \max_{\text{cycle}} J^* - \langle \min_{\text{cycle}} J^* \rangle \tag{7}$$

where the Macaulay brackets $\langle\cdot\rangle$ corresponds to the positive part of the minimum value of J^* computed over the cycle. See Appendix A.1 for the sensitivity analysis to the chosen contour for domain integration.

4.5 The partition of strain energy

We propose to use here the partition of strain energy described above to infer driving forces for fatigue crack growth, corresponding to the local elastic strain energy W_e and local plastic strain energy W_p in Equation (4). Because we use here a behavior model combining plasticity and viscosity, we use for sake of simplicity $\underset{\sim}{\varepsilon}_{vp}$ that includes both inelastic strain terms. Using explicit crack growth by conform remeshing technique, it is possible to evaluate the non-local strain energy, defined in Equation (5), in a volume located at the crack tip. This was achieved by a direct evaluation of the averaged strain energy within a half sphere, as depicted in Figure 5(d). The center of the sphere corresponds to the considered point along the crack front, the half-sphere being defined by the direction of crack propagation. When considering sides of the mesh, the half sphere corresponds to a quarter sphere as highlighted in Figure 5(d). This volume of integration is automatically located at the crack tip.

The non-local averaging is achieved with two half-sphere radii set to 250 and 400 µm respectively. These values were chosen consistently with results obtained on notch plasticity (Maurel et al. 2017) and will be discussed in the sequel. See Appendix A.2 for the sensitivity analysis to the mesh size for strain energy analysis.

5 Results

5.1 FEA of strain and stress fields with crack growth

The developed fatigue crack growth methodology combines multiple ingredients to insure a good quality of FEA with the crack propagation. For sake of simplicity, we propose to analyze only one of the potential used to describe plasticity (the "quick" term), so-called plastic strain in the sequel and described by the accumulated variable *evrcum*, see equations in Table 4. This term has been observed to be much higher than the "slow" term for all tested conditions.

Perspective views of accumulated plastic strain has been plotted in Figure 7(a). This figure corresponds to a crack extension of 600 µm on the free side of the specimen and of 1.6 mm on the

mid-plane of the specimen for $\Delta\varepsilon/2 = 0.375\,\%$. First, accumulated plasticity evidences that the whole gage length bears significant plasticity, Figure 7(a). Detailed views are used to highlight notable features resulting from this FEA, of the free surface for the same crack location are presented below. A large plastic area is observed, and despite a rapid transition from minimum mesh size, of 50 µm, to larger mesh size, local variation of plasticity are mostly continuous at few thousands of microns from the crack tip, Figure 7(b).

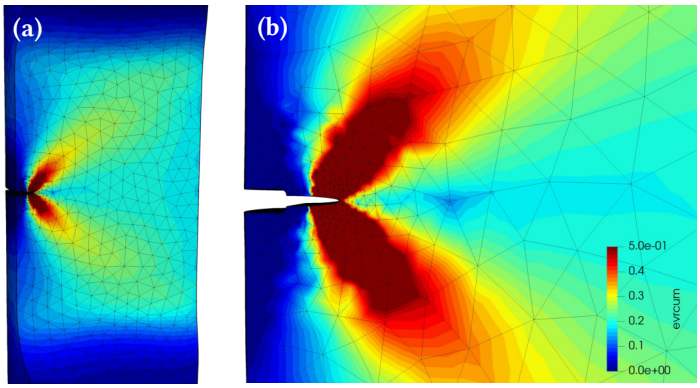

Figure 7 Accumulated plasticity for $\Delta\varepsilon/2 = 0.375\,\%$ and $R_\varepsilon = 0$: (a) perspective view and (b) detailed view of the free surface.

The stress component are known to be very sensitive to the quality of the mesh and FEA. Here detailed view of both Von Mises equivalent stress and trace of stress tensor exhibit continuous field, Figure 8(a) and (b), respectively. If additional dof for pressure convergence was not used, and even using a quadratic mesh, higher stress triaxiality levels together with oscillations from element to element of both stress triaxiality and stress component would have been obtained. Besides, local maximum of the trace of the stress tensor is observed at approximately 2 mm from the crack tip, which is fully consistent with observed micro-crack pattern in front of the major crack tip, see Figure 1. Strain and stress fields confirm that the chosen methodology for field transfer is straightforward in the context of general scale yielding.

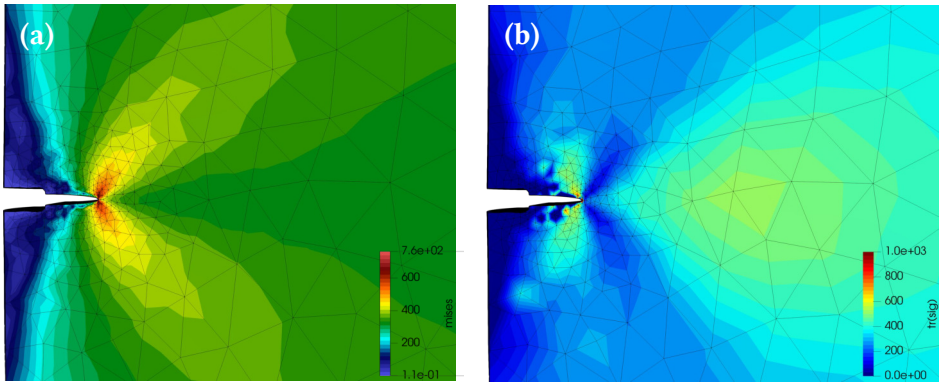

Figure 8 Stress at maximum loading for $\Delta\varepsilon/2 = 0.375\,\%$ and $R_\varepsilon = 0$: (a) Von Mises equivalent stress and (b) Stress tensor trace $\mathrm{tr}\,\sigma$.

A quantitative evaluation of the previous fields has been plotted as a function of the distance from the crack tip r for two levels of loading, for both free surface(s) and mid-plane locations in Figure 9. Von Mises equivalent stress σ_{VM} in Figure 9(a), stress component in the loading direction σ_{22} in Figure 9(c) and accumulated plasticity *evrcum* in Figure 9(d) are monotonically decreasing from the crack tip. While, low stress triaxiality level σ_{H} in Figure 9(b), defined here as $\sigma_{\mathrm{H}} = \mathrm{tr}\,\underset{\sim}{\boldsymbol{\sigma}}/\sigma_{\mathrm{VM}}$, is observed on free surface, close to 0.5, and reaches asymptotic values for distances from the crack tip higher than 1.5 mm. The location of minimum stress triaxiality is function of applied strain level, and is of about 250 µm for $\Delta\varepsilon/2 = 0.125\,\%$ and 500 µm for $\Delta\varepsilon/2 = 0.375\,\%$. At the mid-plane, σ_{H} reaches its highest values, and decreases monotonically from the crack tip. All these plots correspond to the time of maximum loading, and for all observed quantities, asymptotic values are reached after 1–2 mm distance from the crack tip. It is

worth noting that stress quantities are continuous function of the abscissa. Oscillations are more pronounced for accumulated plasticity which appears to be more sensitive to the chosen projection methodology with crack growth and associated remeshing technique.

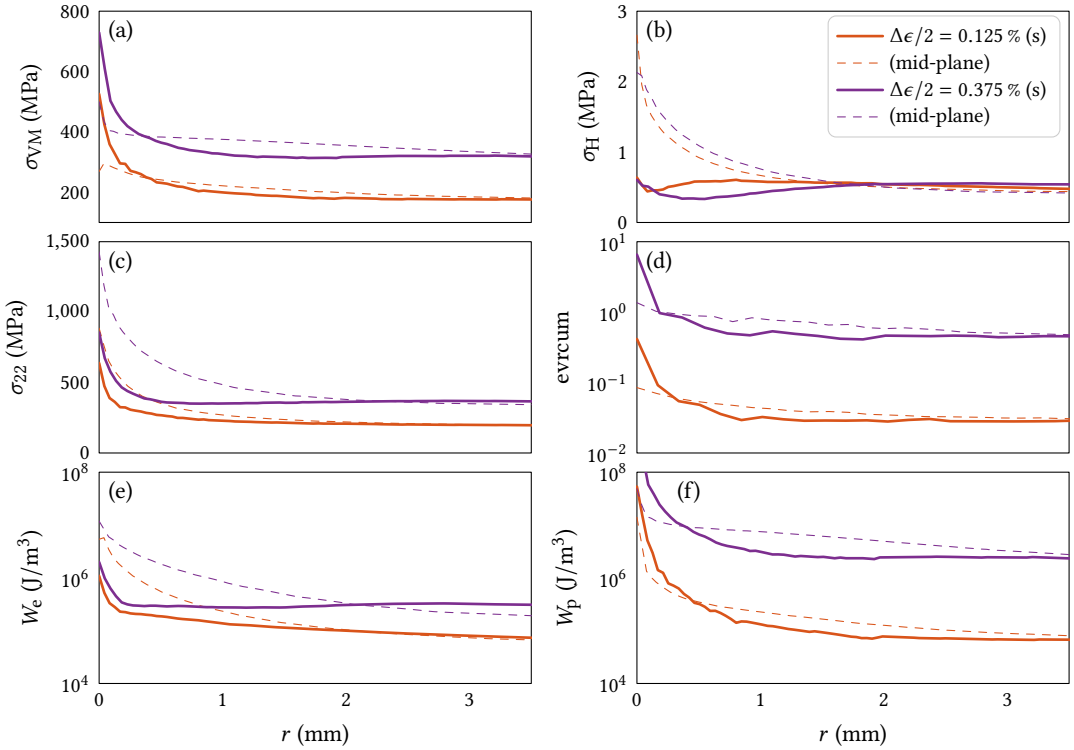

Figure 9 Evolutions of (a) Von Mises equivalent stress σ_{VM}, (b) stress triaxiality σ_H, (c) stress component in the loading direction σ_{22}, (d) accumulated plastic strain 'evrcum', (e) elastic strain energy W_e and (f) plastic strain energy W_p for $R_\epsilon = 0$.

Last but not least, plasticity and higher compressive residual stress level on free surface impacts the crack front curvature (Fessler et al. 2017): the higher the applied strain level, the higher the curvature is assessed. Subsequently, an offset distance is observed between crack tip-location from the surface to the mid-plane of 370 µm for $\Delta\varepsilon/2 = 0.125$ % and of 690 µm for $\Delta\varepsilon/2 = 0.375$ % for the same crack extension on the mid-plane of the specimen (here of 1.25 mm).

5.2 Paris' law from G-θ

ΔJ^* is derived from G-θ as a function of the crack length for each tested loading level, Figure 10(a). Thus, it is possible to determine FCGR using Paris' law based on ΔJ^* evaluation following

$$\frac{\mathrm{d}a}{\mathrm{d}N} = C(\Delta J^*)^m \tag{8}$$

where m and C are the Paris' law parameters adapted to the ΔJ^* analysis. They were identified on the applied strain loading corresponding to $\Delta\varepsilon/2 = 0.125$ %. The associated parameters are detailed in Table 5. Using this Paris' law yields excellent evaluation of FCGR for the two lowest applied strain values. This is obvious for the evolution of measured FCGR as a function of ΔJ^*, Figure 10(b). However, the modelled FGCR is one order of magnitude higher than the measured FCGR values for $\Delta\varepsilon/2 \geqslant 0.025$ %. This result is a direct consequence of the limitation of the ΔJ^* analysis as a driving force for crack when plasticity impacts drastically the evaluation of ΔJ^*, i.e., at the transition between large to general scale yielding condition.

It is worth noting that a convergence is observed for the two highest loading conditions, that could have been used to identify the Paris' law parameters, using a much lower value of the C parameter and keeping the same exponent m. However, such an identification would have led to a large underestimation of modelled FCGR in small scale yielding condition, and subsequently a loss of conservatism of the associated approach. Thus, a Paris' law associated to a standard practice to assess ΔJ^* does not fit to FCGR in a large range of loading.

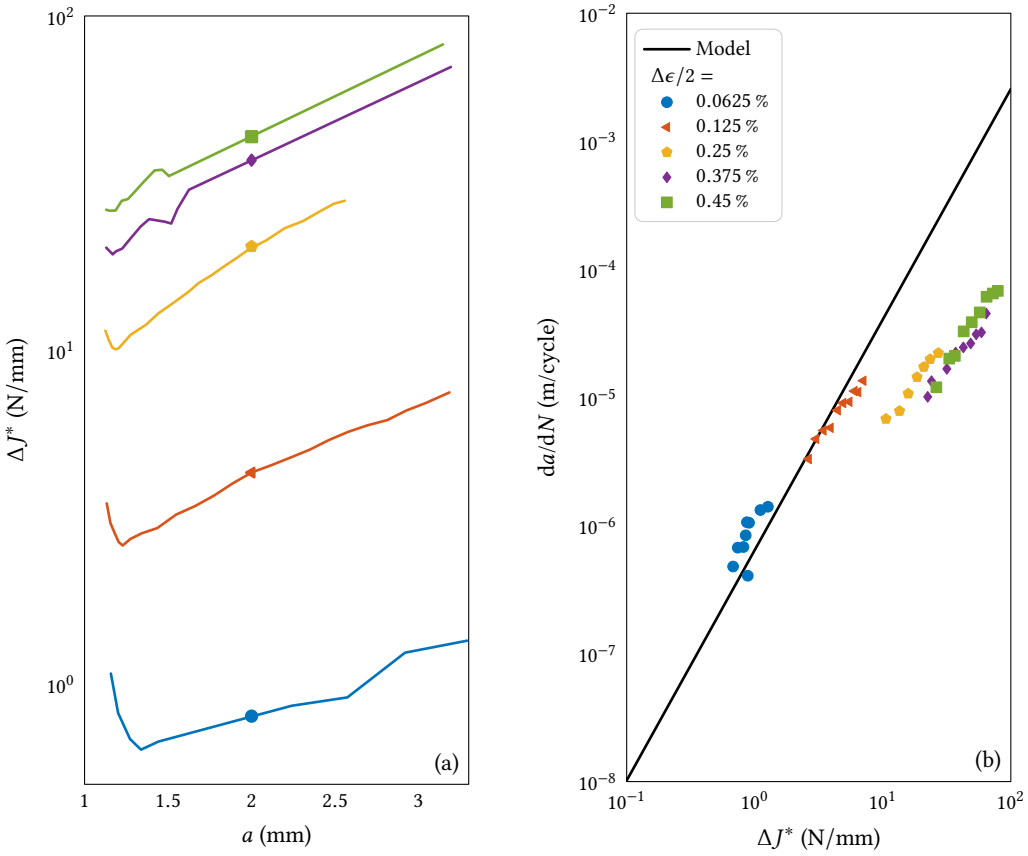

Figure 10 ΔJ and Paris-model assessments. (a) ΔJ^* as a function of crack length a; (b) FCGR as a function of ΔJ^*. Legend symbols common to both subfigures.

5.3 Partition of strain energy in a presence of a crack

Strain energy density As a first result, it is of interest to detail strain energy density field, Figure 11. For sake of figure clarity, the proposed fields correspond to a non-local averaging using a characteristic length of 400 µm. The elastic strain energy density W_e is consistent with the trace of stress tensor pattern, compare Figure 11(a) to Figure 8(b), with global maximum reached at the crack tip and local maximum reached at few millimetres beyond the crack tip. On the other hand, The plastic strain energy density W_p is consistent with plastic strain localization pattern, compare Figure 11(b) to Figure 7. The extension of the area of high level of strain energy density is limited, even though considering free surface of the specimen.

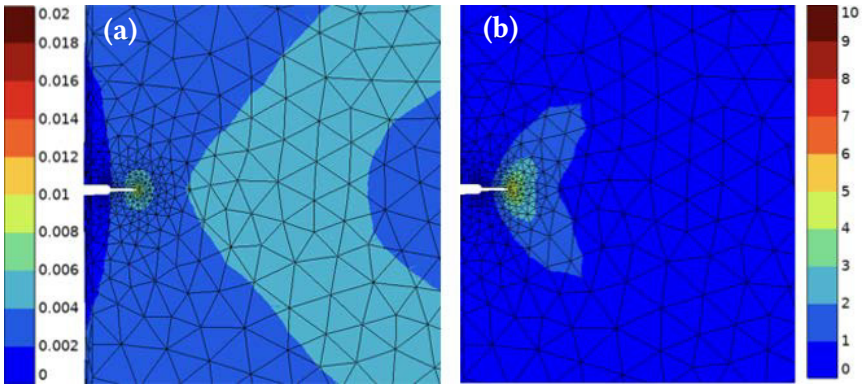

Figure 11 Strain energy density at maximum applied loading using direct non-local field where characteristic length is set to 400 µm: (a) w_e and (b) w_p (values are divided by 10^6 for reading purpose), applied strain level corresponds to $\Delta\epsilon/2 = 0.25\,\%$.

The quantities W_e and W_p are plotted as functions of the distance to the crack tip r in Figure 9(e) and (f), respectively. These plots correspond to the same applied levels as described

previously in Figure 9(a) to (d). The elastic strain energy decreases over a long range distance at the mid-plane location, but it decreases drastically over a similar distance for both applied strain levels on the free surface, limited in the range 200-300 µm, Figure 9(e). The elastic strain energy appears to be strongly correlated to stress component σ_{22}, compare Figure 9(e) to (c).

On the other hand, the plastic strain energy decreases over a distance larger than 1.5 mm for both applied strain levels before reaching asymptotic values. The distance to the crack tip to reach asymptotic values depends of applied strain level and of the considered location (free surface or mid-plane), Figure 9(f). The evolution of plastic strain energy appears to be strongly correlated to the accumulated plastic strain, compare Figure 9(f) to (d).

In the sequel, we choose to test distances for averaging process limiting the impact of such a severe gradient for w_e assessment.

Non-local strain energy as a function of the crack length The chosen quantities of interest, assumed to be driving forces for fatigue crack growth, correspond to the non-local values of strain energy density obtained by averaging in quarter spheres located at the crack tip. Focusing on observable free surface, this quarter sphere is evidenced by the red set of elements in Figure 5(d). The associated strain energy density fields have been highlighted in Figure 11 using inserted views. To ascertain the role of non-local length associated to averaging, two radii have been tested: 250 and 400 µm respectively. These size are consistent with the minimum mesh size set to 50 µm. Accordingly to previous study, oversizing the mesh size for averaging method enables to avoid further mesh dependency (Maurel et al. 2017).

On the one hand, plastic strain energy, w_p, increases with both the crack length and the applied strain level, Figure 12(a). The range of w_p values is here of about three orders of magnitude, see Figure 12(a) using logarithmic scale. This figure being plotted for $a_{tot} = a_0 + \Delta a$, where a_0 corresponds to the notch length. On the other hand, elastic strain energy, w_e, range is narrower than the one observed for w_p, see Figure 12(b) using linear scale, exhibiting a sort of saturation effect for highest applied strain values, consistently with saturation of stress level, Figure 4.

For $\Delta\varepsilon/2 \geqslant 0.125\,\%$, w_p is one order of magnitude higher than w_e, Figure 12(a) and (b). It is worth noting that the evolution of w_p and w_e with the crack length and applied strain level, are similar for both $\ell_c = 250$ µm and $\ell_c = 400$ µm. Consistently with observed gradients and maxima reached at the crack tip, the lower the critical length, the higher the assessed strain energy. Finally, the non-local length used for energy averaging mainly impacts local oscillations for elastic term w_e. The proposed method of averaging prescribes quarter sphere location, with a precision of ± one finite element[1], for which the gradient is the largest, yielding a maximum sensitivity when using $\ell_c = 250$ µm.

5.4 FCGR model based on partition of strain energy

Former FCGR model based on static analysis implies the use of a virtual crack length a, Equation (3). With this, only increase of driving force with crack length could be assessed, unless the loading is actualized with crack growth (Heudt 2013; Dezecot et al. 2019). This point is a strong limitation to structure analysis where driving forces should be assessed in 3D for any crack shape and location in the structure. Thus, we propose here to take advantage of the implicit dependency of strain energy with crack growth to suppress the virtual crack length a from the previous expression. This leads to the new FCGR model

$$\frac{1}{\lambda}\frac{\mathrm{d}a}{\mathrm{d}N} = \left(\frac{w_e}{w_e^*}\right)^{m_e} + \left(\frac{w_p}{w_p^*}\right)^{m_p} \tag{9}$$

where m_e, m_p, w_e^* and w_p^* are the material parameters. λ should be seen as a rationalizing parameter to keep consistent value of w_e^* and w_p^* with obtained energies. For sake of clarity in the comparison of the two critical length, ℓ_c, we chose a priori to set λ to the minimum sphere radius used for averaging, i.e. 250 µm. This model is now independent of the mesh size, by chosen non-local averaging method, and independent a priori of the structure geometry, by a direct

[1] Due to local curvature of the crack tip, the half-sphere being localized by the only abscissa of its centre, some elements are not considered, see Figure 5.

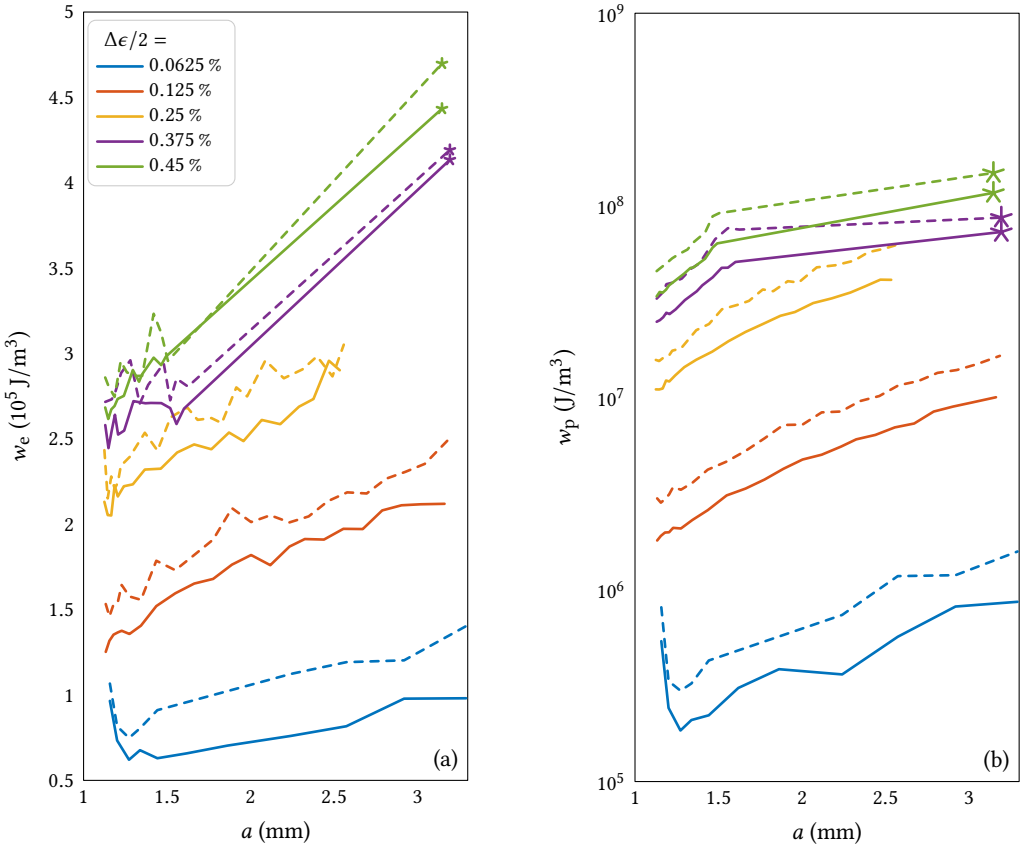

Figure 12 Evolutions with crack length and applied loading of (a) w_e and (b) w_p. Solid and dashed lines correspond to non-local length set to 400 and 250 µm, respectively. Stars correspond to large crack extension as detailed in Section 6.1. Legend common to both subfigures.

evaluation of driving forces for fatigue crack growth thanks to energy terms. See Appendix A.2, for the sensitivity analysis to the mesh size for strain energy analysis and its impact on FCGR.

A simple methodology for the identification of the models parameters is based on the distinction between small and general scale yielding conditions. Assuming that the lowest applied loading, corresponding to $\Delta\varepsilon/2 = 0.0625\,\%$, is mostly driven by the elastic term, namely

$$\frac{1}{\lambda}\frac{\mathrm{d}a}{\mathrm{d}N} = \left(\frac{w_e}{w_e^*}\right)^{m_e} + \left(\frac{w_p}{w_p^*}\right)^{m_p} \simeq \left(\frac{w_e}{w_e^*}\right)^{m_e}, \tag{10}$$

the identification of m_e and w_e^* is obtained by a direct linear regression in the log-log plot of FGCR as a function of w_e, see the solid lines in Figure 13. Similarly, assuming that one of the highest applied loading condition, corresponding to $\Delta\varepsilon/2 = 0.375\,\%$, is mostly driven by the plastic term, namely

$$\frac{1}{\lambda}\frac{\mathrm{d}a}{\mathrm{d}N} = \left(\frac{w_e}{w_e^*}\right)^{m_e} + \left(\frac{w_p}{w_p^*}\right)^{m_p} \simeq \left(\frac{w_p}{w_p^*}\right)^{m_p}, \tag{11}$$

the identification of m_p and w_p^* is obtained by a direct linear regression in the log-log plot of FGCR as a function of w_p, see the dashed lines in Figure 13.

Because of the proposed additive formulation of elastic and plastic contributions to FCGR, the final values of w_e^* and w_p^* are lower than the ones deduced from Equations (10) and (11), respectively. This leads to the model results exposed in Figure 14 and associated model's parameters detailed in Table 5.

The elastic strain energy appears to bring an essential contribution to the quality of the proposed model, this point will be further detailed in the discussion. Whereas, the plastic term is observed to converge to a linear evolution in the log-log plot for both minimum and maximum applied loads. It is worth noting that the plastic contribution could have been identified by fitting

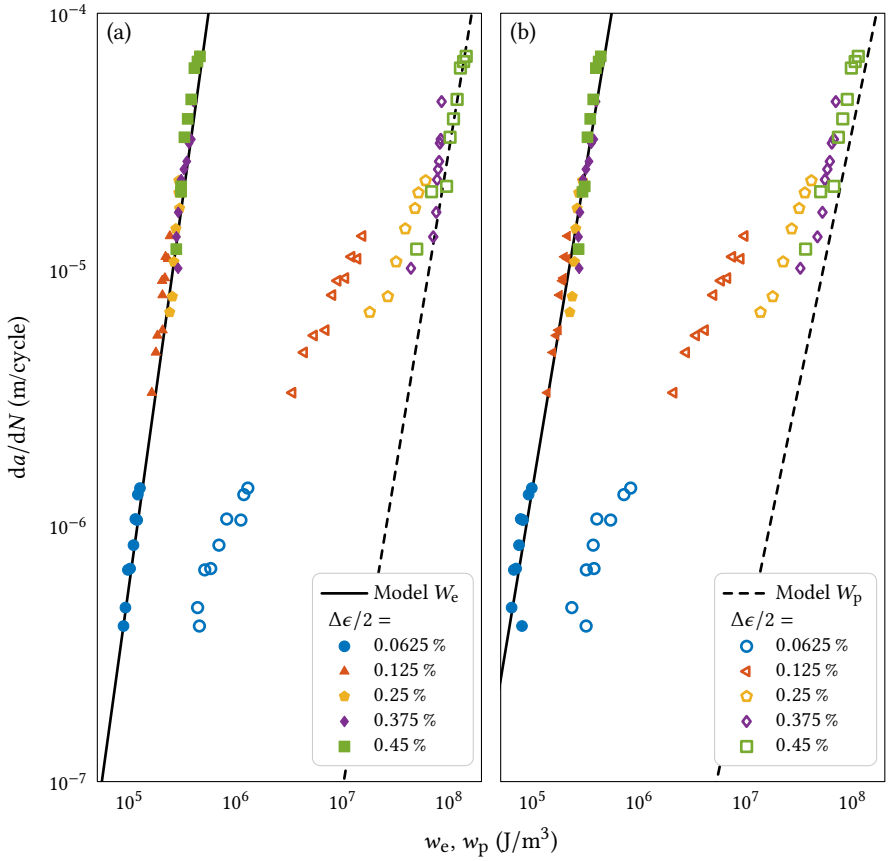

Figure 13 Identification of FCGR function of w_e (filled symbols and solid line, Equation (10)) and function of w_p (empty symbols and dashed line, Equation (11)): (a) $\ell_c = 250\,\mu m$ and (b) $\ell_c = 400\,\mu m$. Legends common to both subfigures.

the minimum applied loading. However, this would have led to loss of consistency with higher applied strain loading, because of the slope difference.

Using strain energy partition method, and summation of both elastic and plastic contribution to FCGR, Equation (9), yields to a pretty good assessment of FCGR for the whole range of applied loading condition, irrespective of the chosen ℓ_c, see Figure 14. This result is a direct consequence of the saturation of elastic strain energy term, w_e, with increasing applied strain loading and the consistency of plastic strain energy term, w_p with observed increase of FCGR with increase in applied strain level $\Delta\varepsilon$.

Besides, this identification is relevant for both small and long crack regimes. Minimum crack modelled corresponds to the crack extension $\Delta a = 200\,\mu m$, which is relative to short crack regime. Final crack length corresponds to a crack extension higher than 2 mm, which is relative to long crack regime. Due to notch plasticity, only for the lowest applied loading, a short crack effect could be associated to local increase in FCGR for $a < 1.3$ mm as compared to $a > 1.3$ mm, Figure 14. The global consistency from short to long crack regimes is observed as a direct benefit of the non-local model developed in this study.

Partition of energy model	[Equation (9)]	ℓ_c (μm)	w_e^* (kJ/m^3)	m_e	w_p^* (MJ/m^3)	m_p
		250	748	3	234	2.5
		400	792	2.5	265	2
Elastic strain energy model	[Equation (13)]	250	647	3		
		400	684	2.5		
Paris's model	[Equation (8)]		C	m		
			9.98×10^{-7}	1.8		

Table 5 FCGR model parameters identified with the set of tested conditions described in Table 3, here $\lambda = 250\,\mu m$.

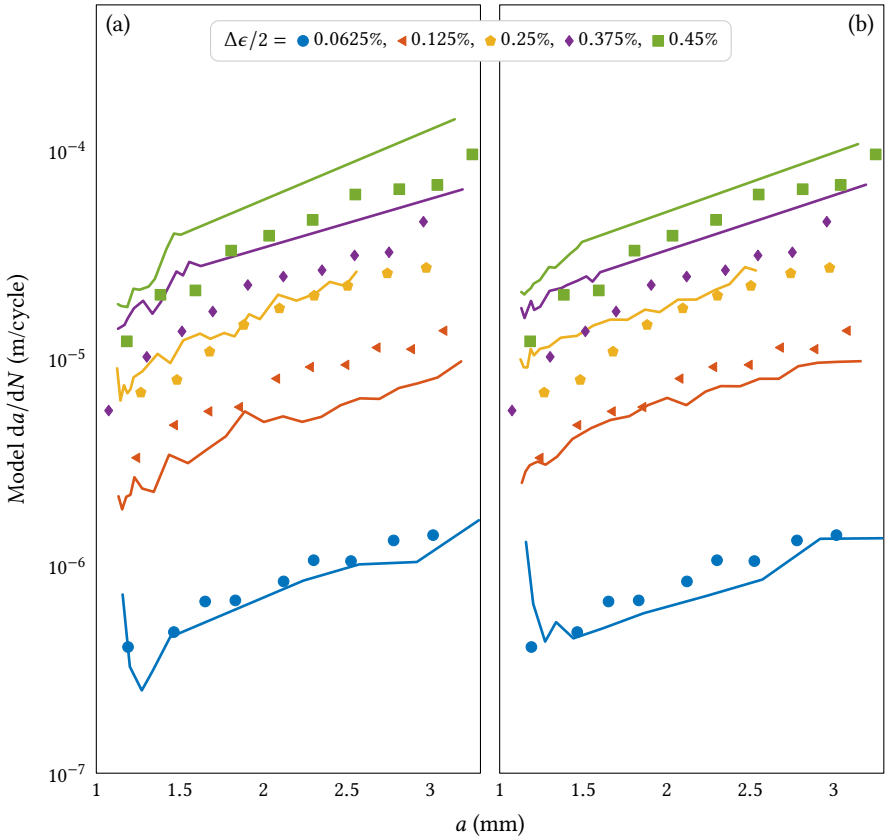

Figure 14 FCGR as a function of crack length a using complete model, Equation (9), experimental fatigue crack growth (symbols) and identified model (lines): (a) $\ell_c = 250\,\mu m$ and (b) $\ell_c = 400\,\mu m$.

6 Discussion

6.1 Crack propagation and plastic wake impact on driving forces

The chosen methodology for fatigue crack propagation implies the projection step in order to consider history during crack growth: plastic wake and associated residual stress field are thus accounted for. To question the optimal computation time, this should be analyzed through relevant strategy of FEA for long crack. Should all crack increments been calculated? or could we introduce a priori any crack length, and through slight crack increment be confident with crack driving forces? This point is of particular interest for complex structure analysis, where lengthy time cost could be prohibitive.

As an example, we use the case $\Delta\varepsilon/2 = 0.25\,\%$ described above, corresponding to the transition to general scale yielding. The rather limited level of plasticity and subsequent reasonable CPU time, make this case of interest. A crack increment of 600 µm is considered derived from above computation. That is to say that for this crack increment, we only used the corresponding mesh, ignoring any prior history, starting computation of crack growth from a natural stress state from this point.

The evolution of ΔJ^* from this point starts from a clear maximum, strongly over-evaluating the ΔJ^* assessed by continuous crack increment analyzed above, see Figure 15(a). After five to six new crack increments from this point, the ΔJ^* assessment is similar for both crack analysis from new crack location and from initial starting crack. One could consider that, this point highlights the relevancy of the proposed scheme of crack growth analysis.

On the other hand, the strain energy terms converge to the continuous crack growth analysis after only one step of crack increment, see Figures 15(b) and (c). This is obvious for both plastic and elastic terms, despite local oscillations associated to scatter already described with elastic term. These results correspond to $\ell_c = 250\,\mu m$, this being the most critical case.

This sensitivity analysis to the starting point of crack reveals two major points: the plastic wake influence on J-integral could be analyzed after 5 to 6 crack increments, whereas, a single

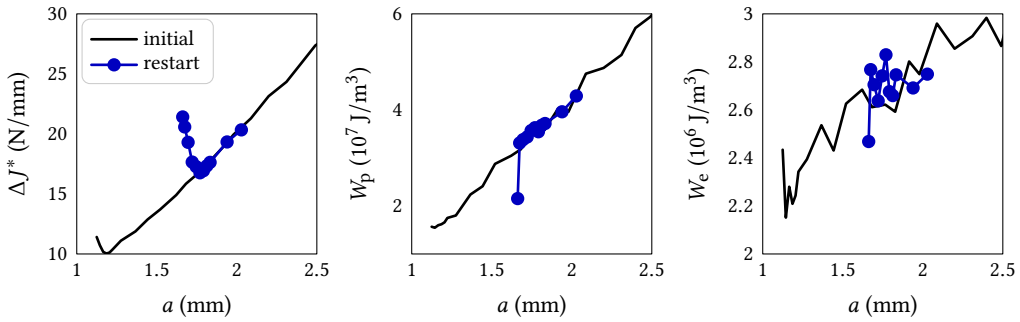

Figure 15 Quantities (a) ΔJ^*, (b) W_p and (c) W_e as functions of the crack length, from initial crack and from a crack increment of 600 µm for $\Delta\varepsilon/2 = 0.25\,\%$ ($\ell_c = 250\,\mu$m).

crack increment is sufficient to get excellent assessment of strain energy density for both elastic and plastic terms. Thus any error in the size of a crack used for structure analysis should be of a lower impact considering the strain energy model proposed in this study as compared to classical J-integral model. This point could be related to the chosen strategy for location/orientation of the half-sphere used for energy averaging: the associated volume is not directly impacted by the contact behavior, because the crack lips are not included in the considered volume for integration. Thus, the considered values of strain energies are mainly associated to the so-called process zone associated to the elaboration of damage at the crack tip in fatigue.

We applied this method to assess ΔJ^*, w_p and w_e for the two maximum applied strain values, $\Delta\varepsilon/2 = 0.375\,\%$ and $0.45\,\%$ respectively, for the maximum crack length tested. These points are highlighted by star-markers in Figures 12 and 15(a).

6.2 Role of elastic and plastic strain energy in FCGR

For the new FCGR model proposed in Equation (9), the relative weight of elastic and plastic strain energies in FCGR has to be investigated. If one considers that the total FCGR $\mathrm{d}a/\mathrm{d}N = v = v_e + v_p$ in Equation (9) is driven by the summation of the elastic and plastic terms, respectively

$$v_e = \lambda\left(\frac{w_e}{w_e^*}\right)^{m_e} \quad \text{and} \quad v_p = \lambda\left(\frac{w_p}{w_p^*}\right)^{m_p} \tag{12}$$

where the ratio $v_e/(v_e + v_p) = v_e/v$ corresponds to the relative weight of v_e to the total FCGR v. The averaged value of this ratio has been plotted as a function of the applied strain level, Figure 16. It is obvious that for the lowest applied strain level, $\Delta\varepsilon/2 = 0.0625\,\%$, v_e/v is close to unity,

Figure 16 Evolution of the ratio between FCGR related to elastic term v_e and FCGR complete model using partition of energy v.

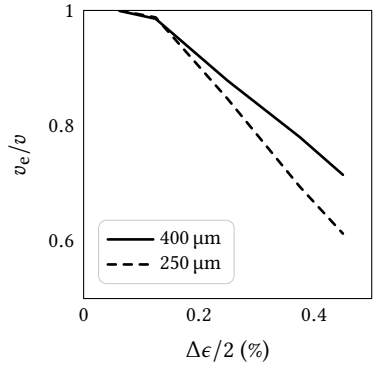

denoting a major influence of elastic strain energy onto FCGR. This is fully consistent with both identification method and with the fact that elastic strain energy is proportional to the square of stress amplitude, namely $w_e \simeq 1/2\sigma^2/E$, making v_e similar in its formulation to a classical Paris' law.

On the other hand, for higher applied strain values, and general scale yielding condition, the elastic contribution on FCGR, v_e term, decreases down to 65 % of the total FCGR for $\ell_c = 250\,\mu$m, but only to 75 % of the total FCGR for $\ell_c = 400\,\mu$m. Despite the chosen identification methodology,

using $\Delta\varepsilon/2 = 0.375\,\%$ to obtain a first evaluation of v_p parameters—namely w_p^* and m_p—the elastic term v_e contributes to a large extent in the quality of FCGR model. Thus we propose to assess FCGR using only the elastic term

$$\frac{1}{\lambda}\frac{\mathrm{d}a}{\mathrm{d}N} = \left(\frac{w_\mathrm{e}}{w_\mathrm{e}^*}\right)^{m_\mathrm{e}}. \tag{13}$$

The obtained identifications of this simplified model are plotted in Figure 17. It is obvious that despite some local oscillations, this model yields a very good assessment of experimental FCGR in comparison with standard ΔJ and Paris' law. Besides, the partition of strain energy into

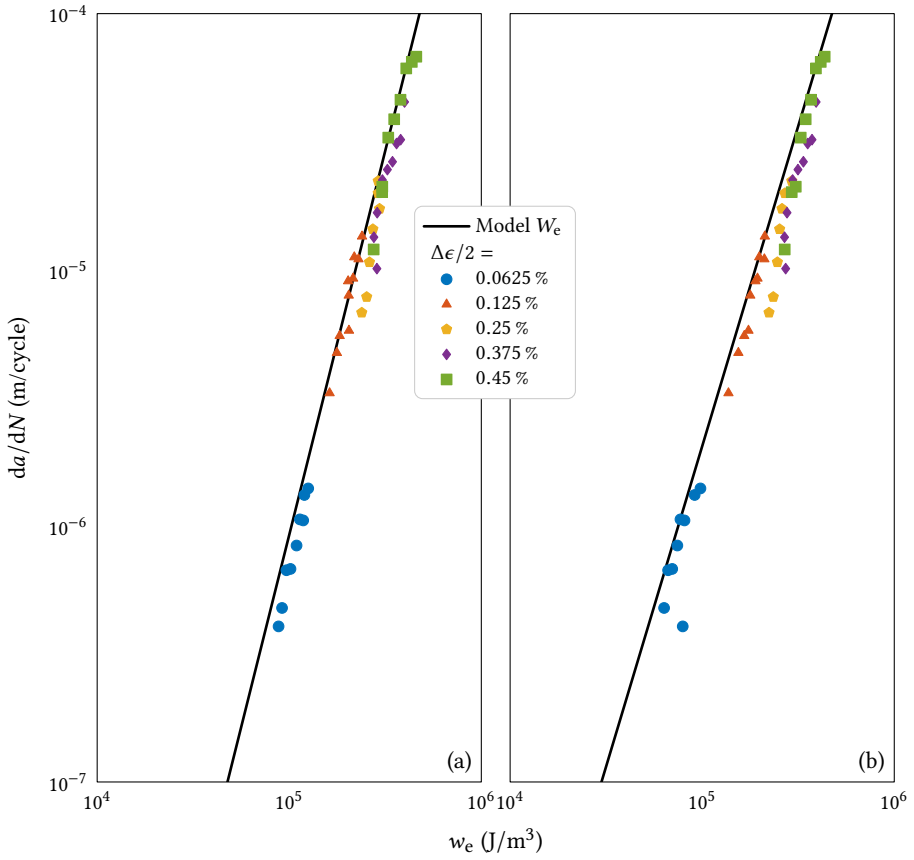

Figure 17 FCGR as a function of w_e: (a) $\ell_c = 250\,\mu\mathrm{m}$; (b) $\ell_c = 400\,\mu\mathrm{m}$.

elastic and plastic terms has enabled a clear identification of driving forces: the elastic term is the dominant driving force for fatigue crack growth, the plastic term being mostly dissipated into heat and diffuse damage. In addition to what, this is worth noting that this conclusion is consistent with most of the work accounting for plasticity in fatigue crack propagation: the crack evolves in a residual stress field induced by plasticity. This means that the quality of stress field assessment, using additional dof to control the pressure field P_n, is a key point of the chosen methodology.

On the other hand, the poor correlation of ΔJ to the FCGR could be related to the contribution of plastic work in its evaluation. It is still complex to extract from the term *grad u* in Equation (6), the elastic and plastic contributions for a general mechanical behavior model. Whereas, this operation is clarified by the partition of strain energy developed above.

7 Conclusions

This paper has proposed a global methodology to assess fatigue crack growth rate from small scale yielding to general scale yielding conditions. It was supported by a complete numerical scheme using remeshing techniques and projection of internal variable fields, including additional dof to reach convergence of the pressure field. This step was seen to be successful considering the quality of stress and strain fields obtained after crack growth.

Based on this numerical assessment of stress and strain fields, both energy release rate and strain energy quantities have been analyzed. Then, a Paris' like model, using only ΔJ^* values derived from G-θ-method, yields large overestimation of FCGR for large and general scale yielding conditions. The proposed original FCGR model based on strain energy partitioning, was adapted from a previous analysis initially developed without crack modeling. Together with a non-local averaging of strain energies, this new FCGR model yields a significant improve of FCGR assessment for a large range of applied strain loading levels. Last but not least, considering only the elastic contribution derived from energy partitioning has led to a simplified and promising model for FCGR.

Complementary works are underway to take into consideration the role of modal mixity on FCGR considering large scale yielding condition.

A Driving forces sensitivity analysis

A.1 Dependency of ΔJ^* to chosen domain

To analyze the ΔJ^* dependency to the chosen domain of integration, extreme values have been plotted in the range of loading tested in this study: $\Delta\varepsilon/2 = 0.0625\,\%$ and $\Delta\varepsilon/2 = 0.45\,\%$. Two domains have been plotted, corresponding to a radius of 0.3 mm and 1.2 mm respectively, as illustrated in Figure A.1.

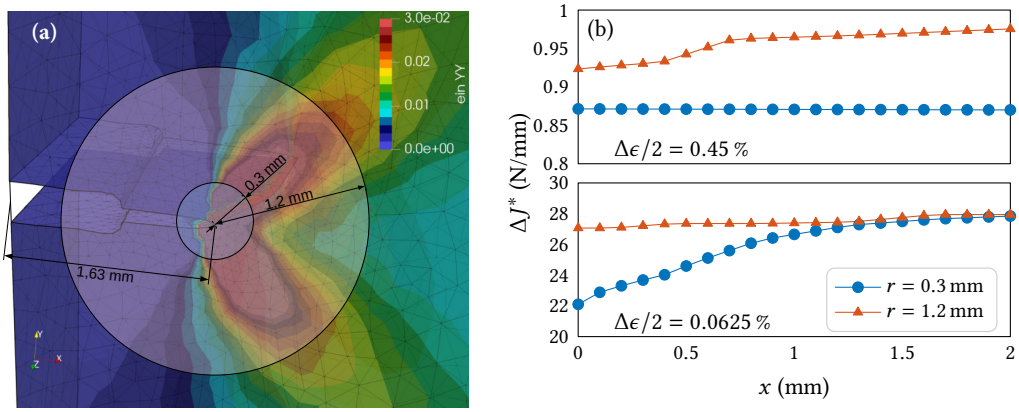

Figure A.1 Dependency of ΔJ^* to the chosen domain size a for loading corresponding to $\Delta\varepsilon/2 = 0.45\,\%$: (a) surface representation of the chosen domain radius; (b) ΔJ^* for two domains and two loads; x describes the location along the crack front, $x = 0$ corresponds to the free surface.

The maximum difference is observed accordingly to the free surface effect, for maximum applied loading and is less than 20 %. Whereas it is obvious that at the middle of the specimen no effect of the size of the domain of integration is observed. Last but not least, in small scale yielding, despite very large differences in chosen domains, a very good path-independence of ΔJ^* is reached.

A.2 Dependency to the mesh size

To analyze the driving forces dependency to the mesh size, a simple case has been tested: it corresponds to pure tension, at the transition from small to large scale yielding, ie $\Delta\varepsilon/2 = 0.25\,\%$. Figure A.2 shows the results of the domain dependency of the three driving force parameters computed at mid-thickness with three elements, and for two characteristic domain lengths, namely $\ell_c = 250$ and 400 µm consistently to the above analysis. Ratios are plotted from the values found for a minimum mesh size of $h = 25$ µm. All quantities evolve with the mesh size. The highest impact is observed for w_p with a linear decrease of values with the mesh size for $\ell_c = 250$ µm. The error being non-linear but more limited for $\ell_c = 400$ µm. For the mesh size of 50 µm chosen in this study, the variation is less than 10 % on strain energy values, for both $\ell_c = 250$ and 400 µm. This induces a possible variation on FCGR lower than 5 % with the identified model based on energy partitioning.

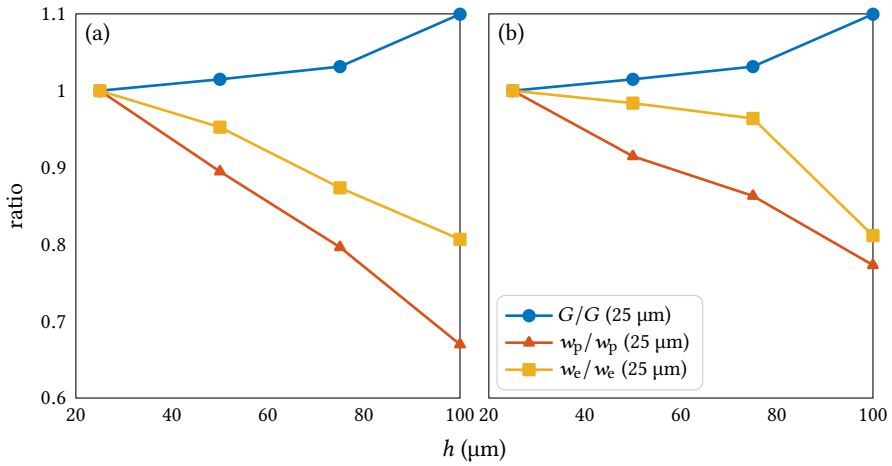

Figure A.2 Sensitivity to the mesh size h for (a) $\ell_c = 250\,\mu m$ and (b) $\ell_c = 400\,\mu m$. Legend common to both subfigures.

References

Benzerga, A. A., J. Besson, and A. Pineau (1999). Coalescence-controlled anisotropic ductile fracture. *Journal of Engineering Materials and Technology* 121(2):221–229. [DOI], [HAL].

Bhanu Sankara Rao, K., M. G. Castelli, G. P. Allen, and J. Ellis (1997). A critical assessment of the mechanistic aspects in HAYNES 188 during low-cycle fatigue in the range 25 °C to 1000 °C. *Metallurgical and Materials Transactions A* 28(2):347–361. [DOI].

Bhanu Sankara Rao, K., H. Schiffers, H. Schuster, and H. Nickel (1988). Influence of time and temperature dependent processes on strain controlled low cycle fatigue behavior of alloy 617. *Metallurgical Transactions A* 19(2):359–371. [DOI].

Chaboche, J.-L. (1993). Cyclic viscoplastic constitutive equations, part I: A thermodynamically consistent formulation. *Journal of Applied Mechanics* 60(4):813–821. [DOI], [HAL].

Chaboche, J.-L., A. Gaubert, P. Kanouté, A. Longuet, F. Azzouz, and M. Mazière (2013). Viscoplastic constitutive equations of combustion chamber materials including cyclic hardening and dynamic strain aging. *International Journal of Plasticity* 46:1–22. [DOI], [HAL].

Charkaluk, E., A. Bignonnet, A. Constantinescu, and K. Dang Van (2002). Fatigue design of structures under thermomechanical loadings. *Fatigue & Fracture of Engineering Materials & Structures* 25(12):1199–1206. [DOI], [HAL].

Chiaruttini, V., D. Geoffroy, V. Riolo, and M. Bonnet (2012). An adaptive algorithm for cohesive zone model and arbitrary crack propagation. *European Journal of Computational Mechanics* 21(3-6):208–218. [DOI], [OA].

Coffin, L. F. (1954). A study of the effects of cyclic thermal stresses in a ductile metal. *Journal of Fluids Engineering* 76(6):931–949. [DOI], [HDL].

Cojocaru, D. and A. Karlsson (2009). Assessing plastically dissipated energy as a condition for fatigue crack growth. *International Journal of Fatigue* 31(7):1154–1162. [DOI], [OA].

Cussac, P. (2020). Influence d'imperfections surfaciques sur la tenue en fatigue de composants nucléaires. French. PhD thesis. France: Ecole nationale supérieure de mécanique et d'aéronautique. [OA].

Cussac, P., C. Gardin, V. Pelosin, G. Hénaff, L. de Baglion, O. Ancelet, and S. Courtin (2020). Low-cycle fatigue crack initiation and propagation from controlled surface imperfections in nuclear steels. *International Journal of Fatigue* 139:105703. [DOI], [HAL].

Destuynder, P., M. Djaoua, and S. Lescure (1981). *Quelques remarques sur la mécanique de la rupture élastique*. French. Tech. rep. EDF–82H335387. Electricité de France. [OA].

Dezecot, S., V. Maurel, J.-Y. Buffière, F. Szmytka, and A. Köster (2017). 3D characterization and modeling of low cycle fatigue damage mechanisms at high temperature in a cast aluminum alloy. *Acta Materialia* 123:24–34. [DOI], [HAL].

Dezecot, S., M. Rambaudon, A. Köster, F. Szmytka, V. Maurel, and J.-Y. Buffière (2019). Fatigue crack growth under large scale yielding condition in a cast automotive aluminum alloy. *Materials Science and Engineering: A* 743:87–97. [DOI], [HAL].

Distene (2021). *Meshgems software*. Version 2.8. [URL].

Doring, R., J. Hoffmeyer, T. Seeger, and M. Vormwald (2006). Short fatigue crack growth under nonproportional multiaxial elastic–plastic strains. *International Journal of Fatigue* 28(9):972–982. [DOI].

Doudard, C., S. Calloch, P. Cugy, A. Galtier, and F. Hild (2005). A probabilistic two-scale model for high-cycle fatigue life predictions. *Fatigue & Fracture of Engineering Materials & Structures* 28(3):279–288. [DOI], [HAL].

Dowling, N. and J. Begley (1976). Fatigue crack growth during gross plasticity and the *J*-integral. *Mechanics of Crack Growth*. Eighth National Symposium on Fracture Mechanics (Brown University, Providence, USA, Aug. 26, 1974–Aug. 28, 1974). ASTM International. [DOI].

Fessler, E., E. Andrieu, V. Bonnand, V. Chiaruttini, and S. Pierret (2017). Relation between crack growth behaviour and crack front morphology under hold-time conditions in DA Inconel 718. *International Journal of Fatigue* 96:17–27. [DOI], [HAL].

Haddar, N., Y. Kchaou, and A. Köster (2013). Numerical computation of the energetic criterion at isothermal and thermal–mechanical cyclic tests under generalized plasticity of the F17TNb stainless steel. *Engineering Fracture Mechanics* 107:1–13. [DOI].

Haigh, J. and R. Skelton (1978). A strain intensity approach to high temperature fatigue crack growth and failure. English. *Materials Science and Engineering* 36(1):133–137. [DOI].

Heudt, A. (2013). Etude de la fissuration en plasticité généralisée. French. PhD thesis. France: Mines ParisTech.

Kamaya, M. (2015). Low-cycle fatigue crack growth prediction by strain intensity factor. *International Journal of Fatigue* 72:80–89. [DOI].

Kolednik, O., R. Schöngrundner, and F. D. Fischer (2014). A new view on J-integrals in elastic–plastic materials. *International Journal of Fracture* 187(1):77–107. [DOI].

Lee, W. Y., I. G. Wright, B. A. Pint, Y. Zhang, and P. K. Liaw (1998). Effects of sulfur impurity on the scale adhesion behavior of a desulfurized Ni-based superalloy aluminized by chemical vapor deposition. *Metallurgical and Materials Transactions A* 29(3):833–841. [DOI].

Manson, S. (1953). *Behavior of materials under conditions of thermal stress*. Tech. rep. NACA-TR-1170. [URL].

Maurel, V., A. Köster, L. Rémy, M. Rambaudon, D. Missoum-Benziane, V. Fontanet, F. Salgado-Goncalves, A. Heudt, H. Wang, and M. Trabelsi (2017). Fatigue crack growth under large scale yielding condition: the need of a characteristic length scale. *International Journal of Fatigue* 102:184–201. [DOI], [HAL].

Maurel, V., L. Rémy, F. Dahmen, and N. Haddar (2009). An engineering model for low cycle fatigue life based on a partition of energy and micro-crack growth. *International Journal of Fatigue* 31(5):952–961. [DOI], [HAL].

Maurel, V., V. Chiaruttini, M. Abecassis, A. Köster, and S. Dezecot (2020). Influence of a 3D realistic crack path in the driving forces for fatigue crack growth under mode I+II loading. *Theoretical and Applied Fracture Mechanics* 108:102570. [DOI], [OA].

McMillan, J. and R. Pelloux (1970). Fatigue crack propagation under programmed loads and crack tip opening displacements. *Engineering Fracture Mechanics* 2(1):81–84. [DOI].

Miller, K. J. (1982). The short crack problem. *Fatigue & Fracture of Engineering Materials & Structures* 5(3):223–232. [DOI].

Mines ParisTech and ONERA (2021). *Zset software, Non-linear material & structure analysis suite*. Version 9.1.3. [URL].

Nittur, P., A. Karlsson, and L. Carlsson (2013). Implementation of a plastically dissipated energy criterion for three dimensional modeling of fatigue crack growth. *International Journal of Fatigue* 54:47–55. [DOI], [OA].

Nittur, P., A. Karlsson, and L. Carlsson (2014). Numerical evaluation of Paris-regime crack growth rate based on plastically dissipated energy. *Engineering Fracture Mechanics* 124-125:155–166. [DOI], [OA].

Ochensberger, W. and O. Kolednik (2015). Physically appropriate characterization of fatigue crack propagation rate in elastic–plastic materials using the J-integral concept. *International Journal of Fracture* 192(1):25–45. [DOI].

Ravi Chandran, K. (2018). Mechanics of fatigue crack growth under large-scale plasticity: A direct

physical approach for single-valued correlation of fatigue crack growth data. *International Journal of Fatigue* 117:299–313. [DOI].

Ribeaucourt, R., M.-C. Baietto-Dubourg, and A. Gravouil (2007). A new fatigue frictional contact crack propagation model with the coupled X-FEM/LATIN method. *Computer Methods in Applied Mechanics and Engineering* 196(33-34):3230–3247. [DOI].

Schweizer, C., T. Seifert, B. Nieweg, P. von Hartrott, and H. Riedel (2011). Mechanisms and modelling of fatigue crack growth under combined low and high cycle fatigue loading. *International Journal of Fatigue* 33(2):194–202. [DOI], [OA].

Shih, C. F. and J. W. Hutchinson (1976). Fully plastic solutions and large scale yielding estimates for plane stress crack problems. *Journal of Engineering Materials and Technology* 98(4):289–295. [DOI].

Simha, N., F. Fischer, G. Shan, C. Chen, and O. Kolednik (2008). J-integral and crack driving force in elastic–plastic materials. *Journal of the Mechanics and Physics of Solids* 56(9):2876–2895. [DOI].

Smith, K. (2011). Application of the dissipated energy criterion to predict fatigue crack growth of Type 304 stainless steel following a tensile overload. *Engineering Fracture Mechanics* 78(18):3183–3195. [DOI].

Suo, X.-Z. and A. Combescure (1992). On the application of $G(\theta)$ method and its comparison with De Lorenzi's approach. *Nuclear Engineering and Design* 135(2):207–224. [DOI].

Tanaka, K., T. Hoshide, and N. Sakai (1984). Mechanics of fatigue crack propagation by crack-tip plastic blunting. *Engineering Fracture Mechanics* 19(5):805–825. [DOI].

Tomkins, B. (1968). Fatigue Crack Propagation an Analysis. *Philosophical Magazine* 18(155):1041–1066. [DOI].

Trabelsi, M. (2019). Propagation de fissures en fatigue oligocyclique multiaxiale à haute température pour le superalliage HAYNES® 188. French. PhD thesis. France: Mines ParisTech. [OA].

Vattré, A. and V. Chiaruttini (2022). Singularity-free theory and adaptive finite element computations of arbitrarily-shaped dislocation loop dynamics in 3D heterogeneous material structures. *Journal of the Mechanics and Physics of Solids* 167:104954. [DOI], [HAL].

Vormwald, M. and T. Seeger (1991). The consequences of short crack closure on fatigue crack growth under variable amplitude loading. *Fatigue & Fracture of Engineering Materials & Structures* 14(2-3):205–225. [DOI].

Vormwald, M. (2013). Elastic-plastic fatigue crack growth. *Advanced Methods of Fatigue Assessment*. Springer, pp 391–481. [DOI].

Zhang, Y., E. Lorentz, and J. Besson (2018). Ductile damage modelling with locking-free regularised GTN model. *International Journal for Numerical Methods in Engineering* 113(13):1871–1903. [DOI], [HAL].

Authors' contributions VM designed the FCGR model and wrote the manuscript. VC developed numerical tools for crack remeshing and G-θ analysis, helped draft, write and review the manuscript, and edit figures. AK conceived, designed and executed the experiments. DM-B developed numerical tools to imitate extensometer control and post-process strain energy.

Supplementary Material Raw data in text format for some of the suggested figures is available at the permalink: 10.5281/zenodo.7576704.

Acknowledgements This work was funded by the ANR grant ANR-14-CE07-0037 SEMAFOR. Mariem Trabelsi for surface roughness measurements used in this paper, Jacques Besson for his fruitful help in representation of non-local field of energy, and Lucien Lairinandrasana for careful analysis of the structure of the paper are warmly acknowledged. Alain Köster (1964-2021) designed the whole set of experiments, was the pivot of these works dealing with (among others) fatigue crack growth at high temperature. Regrets are forever.

Ethics approval and consent to participate Not applicable.

Consent for publication Not applicable.

Competing interests None.

Journal's Note JTCAM remains neutral with regard to the content of the publication and institutional affiliations.